Solvent-cast 3D printing of magnesium scaffolds

Dong, J.; Li, Y.; Lin, P.; Leeflang, M. A.; van Asperen, S.; Yu, K.; Tümer, N.; Norder, B.; Zadpoor, A. A.; Zhou, J.

DOI
10.1016/j.actbio.2020.08.002

Publication date
2020

Document Version
Final published version

Published in
Acta Biomaterialia

Citation (APA)
Dong, J., Li, Y., Lin, P., Leeflang, M. A., van Asperen, S., Yu, K., Tümer, N., Norder, B., Zadpoor, A. A., & Zhou, J. (2020). Solvent-cast 3D printing of magnesium scaffolds. *Acta Biomaterialia*, *114*, 497-514. https://doi.org/10.1016/j.actbio.2020.08.002

Acta Biomaterialia 114 (2020) 497–514

Contents lists available at ScienceDirect

Acta Biomaterialia

journal homepage: www.elsevier.com/locate/actbio

Full length article

Solvent-cast 3D printing of magnesium scaffolds

J. Dong[a,*], Y. Li[a], P. Lin[b], M.A. Leeflang[a], S. van Asperen[c], K. Yu[d], N. Tümer[a], B. Norder[e], A.A. Zadpoor[a], J. Zhou[a]

[a] Department of Biomechanical Engineering, Delft University of Technology, Delft 2628 CD, the Netherlands
[b] Department of Engineering Structures, Delft University of Technology, Delft 2628 CN, the Netherlands
[c] Department of Materials Science and Engineering, Delft University of Technology, Delft 2628 CD, the Netherlands
[d] Department of Bionanoscience & Kavli Institute of Nanoscience, Delft University of Technology, Delft 2629 HZ, the Netherlands
[e] Department of Chemical Engineering, Delft University of Technology, Delft 2629 HZ, the Netherlands

ARTICLE INFO

Article history:
Received 10 March 2020
Revised 13 July 2020
Accepted 3 August 2020
Available online 7 August 2020

Keywords:
Additive manufacturing
Magnesium
Scaffold
Solvent-cast
Sintering

ABSTRACT

Biodegradable porous magnesium (Mg) scaffolds are promising for application in the regeneration of critical-sized bone defects. Although additive manufacturing (AM) carries the promise of offering unique opportunities to fabricate porous Mg scaffolds, current attempts to apply the AM approach to fabricating Mg scaffolds have encountered some crucial issues, such as those related to safety in operation and to the difficulties in composition control. In this paper, we present a room-temperature extrusion-based AM method for the fabrication of topologically ordered porous Mg scaffolds. It is composed of three steps, namely (i) preparing a Mg powder loaded ink with desired rheological properties, (ii) solvent-cast 3D printing (SC-3DP) of the ink to form scaffolds with 0 °/ 90 °/ 0 ° layers, and (iii) debinding and sintering to remove the binder in the ink and then get Mg powder particles bonded by applying a liquid-phase sintering strategy. A rheological analysis of the prepared inks with 54, 58 and 62 vol% Mg powder loading was performed to reveal their viscoelastic properties. Thermal-gravimetric analysis (TGA), Fourier transform infrared spectroscopy (FTIR), carbon/sulfur analysis and scanning electron microscopy (SEM) indicated the possibilities of debinding and sintering at one single step for fabricating pure Mg scaffolds with high fidelity and densification. The resulting scaffolds with high porosity contained hierarchical and interconnected pores. This study, for the first time, demonstrated that the SC-3DP technique presents unprecedented possibilities to fabricate Mg-based porous scaffolds that have the potential to be used as a bone-substituting material.

Statement of Significance

Biodegradable porous magnesium scaffolds are promising for application in the regeneration of critical-sized bone defects. Although additive manufacturing (AM) carries the promise of offering unique opportunities to fabricate porous magnesium scaffolds, current attempts to apply the AM approach to fabricating magnesium scaffolds still have some crucial limitations. This study demonstrated that the solvent-cast 3D printing technique presents unprecedented possibilities to fabricate Mg-based porous scaffolds. The judicious chosen of formulated binder system allowed for the negligible binder residue after debinding and the short-time liquid-phase sintering strategy led to a great success in sintering pure magnesium scaffolds. The resulting scaffolds with hierarchical and interconnected pores have great potential to be used as a bone-substituting material.

1. Introduction

The regeneration of critical-sized bone defects remains a clinical challenge and usually necessitates bone grafting materials. However, the current clinically available grafts and most existing synthetic biomaterials do not meet all clinical requirements [1].

* Corresponding author.
E-mail address: J.Dong-5@tudelft.nl (J. Dong).

https://doi.org/10.1016/j.actbio.2020.08.002

Therefore, developing a new generation of suitable bone substitutes is desired. An ideal bone substitute or implant should: (i) be able to degrade *in vivo* within an appropriate time period till the newly grown bone tissue has replaced the substitute's function [2], (ii) exhibit osteogenic, osteoconductive and osteoinductive properties for new bone formation [3], (iii) be biomechanically stable and match the mechanical properties of the host bone to avoid stress shielding [2,3], prior to losing its mechanical functionality, and (iv) present a highly porous structure with fully interconnected pore networks to allow for bone ingrowth and facilitate the transport of nutrients and metabolic waste [4].

In recent years, Mg-based biodegradable metals have been considered to be a new class of promising biomaterials for orthopedic applications, since they may be tuned to possess mechanical and biological performances needed for bone defect regeneration [5]. One of the main advantages of Mg over currently used metallic biomaterials is its biodegradability [5]. Mg ions play an important functional role in physiological systems [6]. Moreover, it has been reported that Mg ions released from Mg implants stimulate bone formation [7]. Additionally, Mg possesses appropriate mechanical properties that are close to those of the natural bone [8]. In other words, Mg-based materials can satisfy the first three requirements mentioned above for biodegradable implants aimed to regenerate bone. Incorporating porosity into Mg-based implants is of critical importance to meet the last requirement of an ideal bone substitute for orthopedic and traumatological applications.

Several techniques to fabricate porous Mg scaffolds have already been developed including melt foaming [9–11], preform infiltration [12–16], pattern casting [17,18], and powder metallurgy with space holder [19–22]. However, these traditional fabrication techniques permit neither complex exterior 3D architectures nor fully interconnected interior networks. Recent advances in additive manufacturing (AM) offer great potential to achieve a much greater degree of design and manufacturing flexibility and efficiency over the traditional techniques, making it possible to design and fabricate fully interconnected porous structures with precisely controlled topological parameters [23,24].

Employing AM techniques to fabricate Mg-based materials has just started in a very small number of university research groups [25]. Selective laser melting (SLM) in the category of powder bed fusion according to the ASTM classification is a commonly chosen AM technique for Mg scaffold fabrication [25–30], compared to other AM techniques [31,32]. The success in fabricating porous Mg alloy scaffolds with SLM is yet rather limited [33,34]. The primary challenge encountered is associated with the safety in operation, considering the high flammability of Mg powder with a large collective surface area. The other difficulties encountered concern the undesirable compositional variation in final parts due to relatively low melting and boiling temperatures of Mg and to rapidly increased vapor pressure of Mg at its boiling temperature [27,35], excessive oxidation throughout the whole chain of scaffold fabrication due to the high affinity of fine Mg-based powder particles to oxygen [27], and seriously limited availability of pre-alloyed Mg powders with desired compositions that can be used to adjust the biodegradation rate and mechanical properties of the porous structures [25]. Furthermore, due to the high reflectivity of Mg powder, high laser power is needed, which makes the SLM equipment costly [27], increases the chance of Mg evaporation, and creates significant thermal gradients during SLM, leading to metallurgical defects and residual stresses [36]. Recently, a few attempts have been made to develop powder bed inkjet 3D printing [37] and fused filament fabrication (FFF) techniques [38], followed by a sintering step, as alternatives to SLM. However, utilizing these techniques for the fabrication of topologically ordered porous Mg scaffolds has not yet been reported.

Solvent-cast 3D printing (SC-3DP) is another interesting technique alternative to SLM, in which an ink containing metallic or any other powder particles, together with a binder system (composed of polymer, volatile solvent, and/or additive), is extruded through a nozzle and printed into a designed structure. The 3D printed structure is then subjected to debinding and sintering. SC-3DP has great potential to overcome the material, technical, and structural limitations of the other AM techniques currently applied to fabricate porous Mg scaffolds, as mentioned earlier. It offers multiple advantages including (i) 3D printing at ambient conditions, (ii) easy adjustment of the components of the ink, (iii) low investment in equipment, and (iv) the potential to fabricate complex structures with hierarchical pores and desired alloy compositions. In addition, in SC-3DP, no natural support is present for overhung parts, which is in contrast to the presence of natural support in powder bed based AM processes. Precise match of the evaporation rate of solvent and printing parameters allows for printing stacked lattice structures with overhang parts and enables the fabrication of helically freeform structures without any synthetic support [39]. The SC-3DP method has been demonstrated to be feasible in the case of the AM of steel [40,41], iron [42,43], titanium-based [44], and nickel-based [43,45,46] micro-trusses.

To the best of our knowledge, there have been no reports on SC-3DP of Mg scaffolds. It is worth noting that unlike relatively less reactive metals, fabricating Mg-based materials through the SC-SDP approach could present a different set of challenges including (i) a limited choice of binder components due to the high reactivity of Mg powder, leading to interactions during the printing and debinding processes and the exclusion of the use of water-based and PLGA-containing binder systems suitable for SC-3DP of other metals, (ii) the poor sinterability of Mg powder in the absence of external pressure, because of the inevitable presence of a stable oxide film on Mg powder particle surface, which acts as a barrier to diffusion.

In the present study, we attempted to overcome these challenges and apply the SC-3DP technique to build topologically ordered biodegradable pure Mg scaffolds. Pure Mg was chosen in this first attempt to make the material system simple and avoid unexpected interactions between the alloying elements and binder. This work was aimed to demonstrate the viability of using the SC-3DP technique to produce Mg scaffolds and to find applicable and optimized process conditions for successfully fabricating porous Mg scaffolds with high fidelity. First, the prepared inks, consisting of a judiciously formulated binder and Mg powder particles, were evaluated in their rheological behavior. Rheological characterization was intended to lay the basis for initial screening of inks prior to time-consuming trials of 3D printing and also to provide quantitative support for the evaluation of printability and for the description of observed behavior during the printing process. Second, the inks with different percentages of Mg powder loading were printed by applying the SC-3DP approach and the applicable printability windows were defined. Finally, the effects of sintering temperature and holding time on the density of struts were investigated in light of maintaining the shape fidelity of the scaffolds.

2. Materials and methods

2.1. Fabrication strategy

The SC-3DP approach to the fabrication of porous Mg scaffolds consisted of three steps (Fig. 1a): ink preparation, 3D printing of Mg scaffolds with a designed structure, and debinding and sintering. First, inks containing a binder system (polymer, volatile solvent, and additive), and different percentages of Mg powder loading were prepared. Second, the prepared ink with the required rheological properties was extruded through a micro-nozzle under

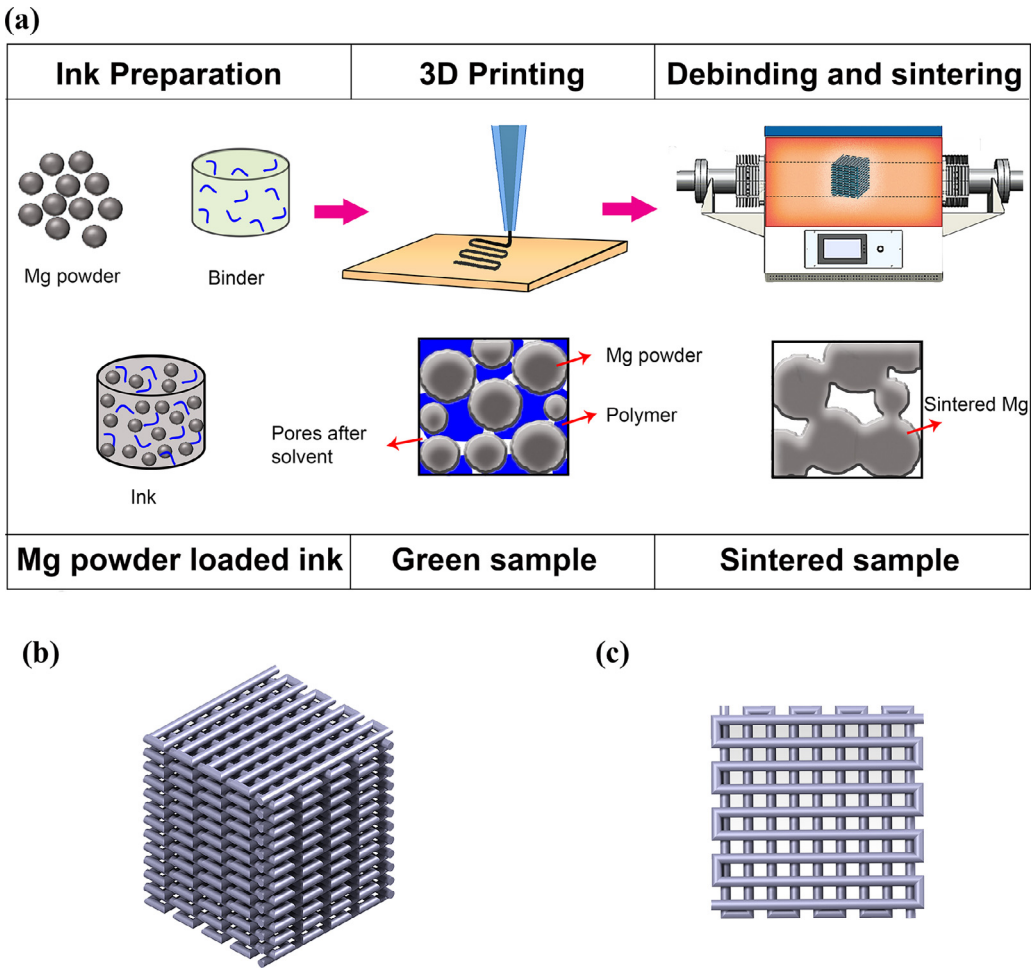

Fig. 1. A schematic diagram of the fabrication steps and the designed structure of Mg scaffolds: (a) the fabrication process consisting of ink preparation, 3D printing, and post-processing, (b) the CAD model of the scaffold, and (c) the lay-down pattern of the scaffold.

an applied pressure and at an appropriate printing speed. The volatile solvents in the extruded struts rapidly evaporated upon extrusion, enabling the condensation of the remaining polymer and increasing the rigidity of the deposited Mg powder loaded struts. This allowed the struts to hold their shape and support the subsequent layers. The presence of the additive prevented the solvent from excessively fast drying, due to its lower vapor pressure, thereby permitting adjacent layers to merge during deposition. Green scaffold samples with Mg powder particles, polymer, and additives were created. Finally, the green scaffold samples were transformed into pure Mg scaffolds through a thermal treatment, during which polymer and additives were thermally decomposed and Mg powder particles were sintered together.

2.2. Ink preparation and characterization

2.2.1. Powder characterization

Atomized pure Mg powder particles with a purity of 99.8 wt% (Zn: 0.0081 wt%, Fe: 0.0085 wt% and others: 0.17 wt%) (Tangshan Weihao Magnesium Powder Co., China) had a particle size range of 25 to 80 μm (D_{10} = 31.11 μm, D_{50} = 44.96 μm and D_{90} = 67 μm). The morphology of the powder was examined with a scanning electron microscope (SEM, JSM-IT100, JEOL, Japan). The microstructure of the Mg powder was observed with an optical microscope (OM, VH-Z250R, KEYENCE, USA) after grinding, polishing, and etching in a solution composed of nitric acid, acetic acid, water, and ethanol at a volume ratio of 1:3:4:12. The average grain size was determined by using the line intercept method.

2.2.2. Ink preparation

Mg powder loaded inks were synthesized through mixing of (i) Mg powder particles and (ii) a binder system composed of polystyrene (Sigma-Aldrich), chloroform (Sigma-Aldrich) and dibutyl phthalate (Sigma-Aldrich). Mg powder particles were added into the already made binder in a glove box to prevent Mg powder particles from being oxidized during ink preparation. Inks with 54, 58, and 62 vol% powder loading were prepared, respectively. The binder and Mg powder mixtures were further mixed by applying magnetic stirring for improvements in homogeneity. The synthesized inks were then centrifuged at 102 rad/s for 1 min and at 25 °C to remove air bubbles.

2.2.3. Rheological characterization

The rheological properties of the 54, 58, and 62 vol% Mg powder loaded inks were determined by using a rheometer (Physica MCR 301, Anton Paar, Germany) with a plate-plate geometry (25 mm diameter, 1 mm distance). A shear stress ramp, ranging from 1 to 10,000 Pa at 1 Hz, was applied to the ink and the linear viscoelastic range (LVR) was determined. Rotational shear rate-viscosity measurements were performed in the flow mode at shear rates varying between 0.1 and 220 s^{-1}. The linear trend when plotting the results on a double-logarithmic scale was fitted into a

power law equation to quantify the degree of shear thinning:

$$\eta = K\dot{\gamma}^{n-1} \quad (1)$$

where η is the viscosity, $\dot{\gamma}$ the shear rate, K the consistency index and n the flow behavior index.

The storage (G') and loss (G'') moduli were obtained from a frequency sweep test over a frequency range of 0.1 to 10 Hz at a constant stress selected from the LVR (τ = 10 Pa). In the creep experiment, a constant shear stress selected within the LVR (τ = 10 Pa) was applied for 60 s and the resulting strain was measured. Then, in the recovery test, the stress was removed and the strain was recorded for another 180 s. The compliance (J) was obtained from the ratio of the measured strain to the applied stress. The degree of recovery (R) of the ink (*i.e.*, the ability to recover from deformation) was calculated as:

$$R = \frac{J_{max} - J_{\infty}}{J_{max}} \quad (2)$$

where J_{max} and J_{∞} are the compliance at the end of the creep and the recovery tests, respectively.

2.3. 3D printing

2.3.1. Flow rate measurement

The 54, 58, and 62 vol% Mg powder loaded inks were transported into plastic syringes (EFD, Nordson, Germany) with a 410 μm tapered nozzle (EFD, Vieweg, Germany), which were mounted on a 3D Bioscaffolder printer (BS 3.2, GeSim, Germany). To determine the flow rates of the inks with different percentages of Mg powder loading, the inks were extruded under applied pressures of 60, 80, 100, and 500 kPa for 5, 10, and 15 min. Because the 62 vol% ink could not be extruded at the applied pressures of 60, 80 or 100 kPa, an additional extrusion pressure of 600 kPa was applied for evaluating 62 vol% ink flow rate. The extruded Mg powder containing struts were collected and weighed using a high-precision balance after drying in a fume hood. Then, the mass flow rate was determined by dividing the total weight (the weight of the evaporated solvents was also included in calculation) of the extruded struts dispensed at various time points along a certain dispensing time (5, 10, or 15 min) to obtain an average mass flow rate. The average volumetric flow rate was then obtained by converting the mass flow rate using the respective ink density. The induced shear rate, as the ink flew through the nozzle tip, was correlated with the flow rate and was estimated by

$$\dot{\gamma} = \frac{3n+1}{4n} \cdot \frac{4\dot{Q}}{\pi R^3} \quad (3)$$

where $\dot{\gamma}$ is the shear rate, R the radius of the nozzle, n the shear-thinning coefficient, and Q the volumetric flow rate.

2.3.2. Scaffold structure design

A cuboidal architecture (dimensions: 7 mm × 7 mm × 8 mm) with a strut size of 410 μm, a spacing distance of 390 μm and a lay-down pattern of 0°/90°/0°(Fig. 1b), and a relative density of 53.7% (the design value, calculated by Solidworks), was designed using the GeSim custom software. A linear infill pattern (Fig. 1c) was adopted for the designed structure, since it is the most reliable pattern to create uniform porous structures and allows for a fast and facile fabrication process. This designed structure was meant to easily and quickly determine the printability of the created Mg powder loaded inks and the formability of the scaffolds, as well as the optimized printing process parameters.

2.3.3. 3D printing and printability window

The 54, 58, and 62 vol% Mg powder loaded inks were extruded under various applied pressures at room temperature. The extruded struts were deposited on a glass slide as the substrate. The distance between the glass slide and the nozzle tip, and the layer height were both set to be 320 μm in the system, which was almost 80% of the inner diameter of the nozzle. Considering the capacity of the printer used, applied pressures ranging between 1 and 600 kPa (the maximum pressure of the printer) and printing speeds varying between 1 and 18 mm/s were used to determine the printability windows of the three Mg powder loaded inks to realize the desired architecture. First, the operating process parameters (applied pressure and printing speed) that enabled the width of extruded struts in a range of 300–500 μm were chosen as the preliminary parameters. Considering the difficulties to obtain the struts having exactly the same diameter as the nozzle size, a relatively large range of 300–500 μm was empirically chosen to make the resultant printing window suitable for different printing cases of Mg scaffolds, since inevitable experimental errors could greatly affect the size of extruded struts during the printing process. Then, these parameters were further screened through building 3D structures and evaluating them. Finally, the printability windows of the inks to fabricate the designed Mg scaffolds were determined. The criteria for the printability of the scaffolds were as follows (i) the deflection degree (δz) of spanned struts must be less than 5% of the extruded struts diameter [47] and (ii) there should be no apparent defects or displacements of the printed struts. After the printability windows were constructed, a number of printing process parameter sets were selected for these zones and marked as A, B, C, D, E and F in the windows, and then the resultant scaffolds were imaged under SEM and taken as the examples.

2.4. Debinding and sintering

The samples with 58 vol% Mg powder loading, struts of 350 ± 10 μm, and an interspace of 450 ± 9 μm, printed with the parameters selected from the defined printability window, were subjected to debinding and sintering. The debinding and sintering processes were conducted in a tube furnace with a controlled atmosphere of high-purity argon (purity ≥ 99.9999%). The printed materials were heated at 5 °C/min from room temperature to 650 °C with various dwelling times (5, 10, and 35 min), followed by furnace cooling to room temperature. To investigate the effect of sintering temperature, part of the 3D printed samples was sintered at 660 and 670 °C.

2.5. Material characterization

To determine the exact temperature of binder removal, thermal-gravimetric analyses (TGA 8000, PerkinElmer, USA) of pure binder samples and green samples with 58 vol% Mg powder loading were conducted by heating the samples to 650 °C at a rate of 5 °C/min and at an Ar flow rate of 40 mL/min. The as-received Mg powder and the as-sintered Mg samples were also subjected to TGA, following the same procedure as above. The analyses were performed in triplicate. The adsorption spectra of the green samples and those heated to 220, 450, and 650 °C were generated using a Fourier transform-infrared spectroscope (FTIR, Spectrum 100, PerkinElmer, USA). A portion of the green sample was placed on the diamond attenuated total reflection (ATR) crystal. The spectra over a range of 4000 to 600 cm^{-1} were obtained by 30 scans with a spectral resolution of 4 cm^{-1}. Phase constituents in pure Mg powder, printed and sintered scaffolds were identified by using an X-ray diffractometer (XRD, Bruker D8 Advance diffractometer Bragg–Brentano geometry). The diffractometer was equipped with a Lynxeye position sensitive detector and operated at 45 kV and 40 mA with a scan range of 10–110° and a step size of 0.030° using Cu Ka radiation. Quantitative analysis of magnesium oxide (MgO) was performed using Bruker software (Diffrac.Suite EVA,

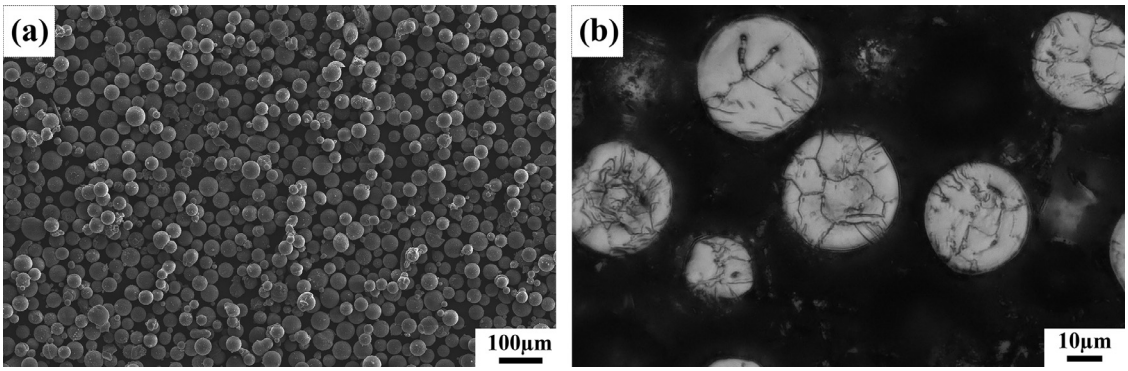

Fig. 2. The characteristics of the Mg powder: (a) a SEM image showing spherical powder particles and (b) the microstructure of the Mg powder.

5.2). Chemical analyses of the as-received Mg powder and sintered parts in terms of carbon content were performed using a carbon/sulfur analyzer (CS744, LECO, USA). Three repeat samples for each group were measured.

The printed 2D pattern and the cross section of the sintered samples were imaged under the optical microscope. The green samples and sintered samples were also examined using SEM. The relative density of the sintered struts was measured from the optical images of the polished cross sections using the ImageJ software (National Institutes of Health, US). The shrinkage of the sintered samples was determined by measuring the dimensions of the samples before and after sintering using a digital caliper. The sintered scaffolds were imaged by using X-ray micro-computed tomography (μCT, Nanotom 180NF, Phoenix) at a current of 140 μA and a voltage of 140 kV, and resolutions of 5 μm and 2 μm. To calculate the porosity, struts size, and pore size of the sintered samples, the scanned images were exported to Fiji (National Institutes of Health, US). The regions of interest (ROIs) were then defined. Subsequently, the BoneJ [48] plugin was used for the calculations.

2.6. Statistical analysis

Statistical analysis was performed using ANOVA (one way or two way) or the Scheirer-Ray-Hare test with post-hoc Tukey's multiple comparison test. $p < 0.05$ was considered statistically significant.

3. Results

3.1. Characteristics of the Mg powder

Atomized pure Mg powder particles appeared to be spherical (Fig. 2a) under SEM, typical of the characteristics of an argon-protected centrifugally atomized powder. On the cross-sections of powder particles, the average grain size was 8.6 ±1.7 μm (Fig. 2b).

3.2. Rheological characteristics of the inks

The viscosity-shear stress curve of each of the three prepared inks (with 54, 58 and 62 vol% Mg powder loading) showed a steep drop in viscosity at a certain shear stress (Fig. 3a). A relative steady region was observed before reaching the critical shear stress, known as the yield stress (τ_y). The yield stress was determined at the intersection of the two tangents: one in the stable region of viscosity where the material was deformed elastically and another in the region where the viscosity dropped and the material started to flow. The yield stress of the ink with a higher percentage of Mg powder loading was higher than that of the ink with a lower percentage of Mg powder loading (Table 1). Fig. 3b shows the decreases in viscosity with increasing shear rate for all the three samples, which is known as the shear-thinning behavior, being of great importance for the inks to be extruded through fine nozzle and at the same time to retain the shape after deposition. Over the full shear rate range, the viscosity value of the ink with a higher percentage of Mg powder loading was higher than that of the ink with a lower percentage of Mg powder loading (Fig. 3b). The shear-thinning degrees of the three inks were similar (Fig. 3b), which could be observed from the fitted results (*i.e.*, the values of the shear-thinning coefficient, n) (Table 1).

Table 1
Rheological parameters of the inks with different percentages of Mg powder loading, in which n is the shear-thinning coefficient and K the consistency index.

Ink	Yield stress (Pa)	n	K	Recovery degree
54 vol% ink	2677 ± 87^a	0.18 ± 0.03^a	240 ± 36^a	$26\% \pm 1\%^a$
58 vol% ink	4753 ± 6^b	0.06 ± 0.01^a	1313 ± 337^a	$29\% \pm 3\%^a$
62 vol% ink	5917 ± 76^c	0.05 ± 0.01^a	6782 ± 419^b	$27\% \pm 3\%^a$

a–c: different lowercase letters represent statistically significant differences between the groups of the different percentages of Mg powder loading at $p < 0.05$ (comparison in column).
The same letter indicates that the values are not significantly different.

The storage (G') and loss (G'') moduli were determined through a frequency sweep test to examine the viscoelastic properties of the prepared inks, which were considered crucial for successful printing. In the frequency sweep testing, both the storage and loss moduli increased with rising Mg powder loading and frequency (Fig. 3c). For all the inks with the three percentages of Mg powder loading, the storage moduli were all higher than the loss moduli, indicating that the inks showed elastic or solid-like behavior, which was necessary for retaining the shape of extruded part and supporting its own weight and the layers on top during SC-3DP. The creep-recovery testing was also performed to characterize the viscoelastic properties of the inks, expressed by the compliance $J(t)$ as a function of time (Fig. 3d). The results showed a nonlinear growth trend in the creep test and an exponential decay in the recovery region. The ink with different Mg powder loading showed similar degree of recovery (Table 1).

3.3. 3D printing

Fig. 4a shows that the flow rates of the inks steadily increased with rising applied pressure. When the flow rates of the inks with different percentages of Mg powder loading at a given applied pressure were compared, the ink with 54 vol% Mg powder loading exhibited the highest flow rate, while the ink with 62 vol% Mg powder loading had the lowest flow rate. It should be noted that the ink with 62 vol% Mg powder loading could not be extruded out of the nozzle when a pressure less than 350 kPa was applied.

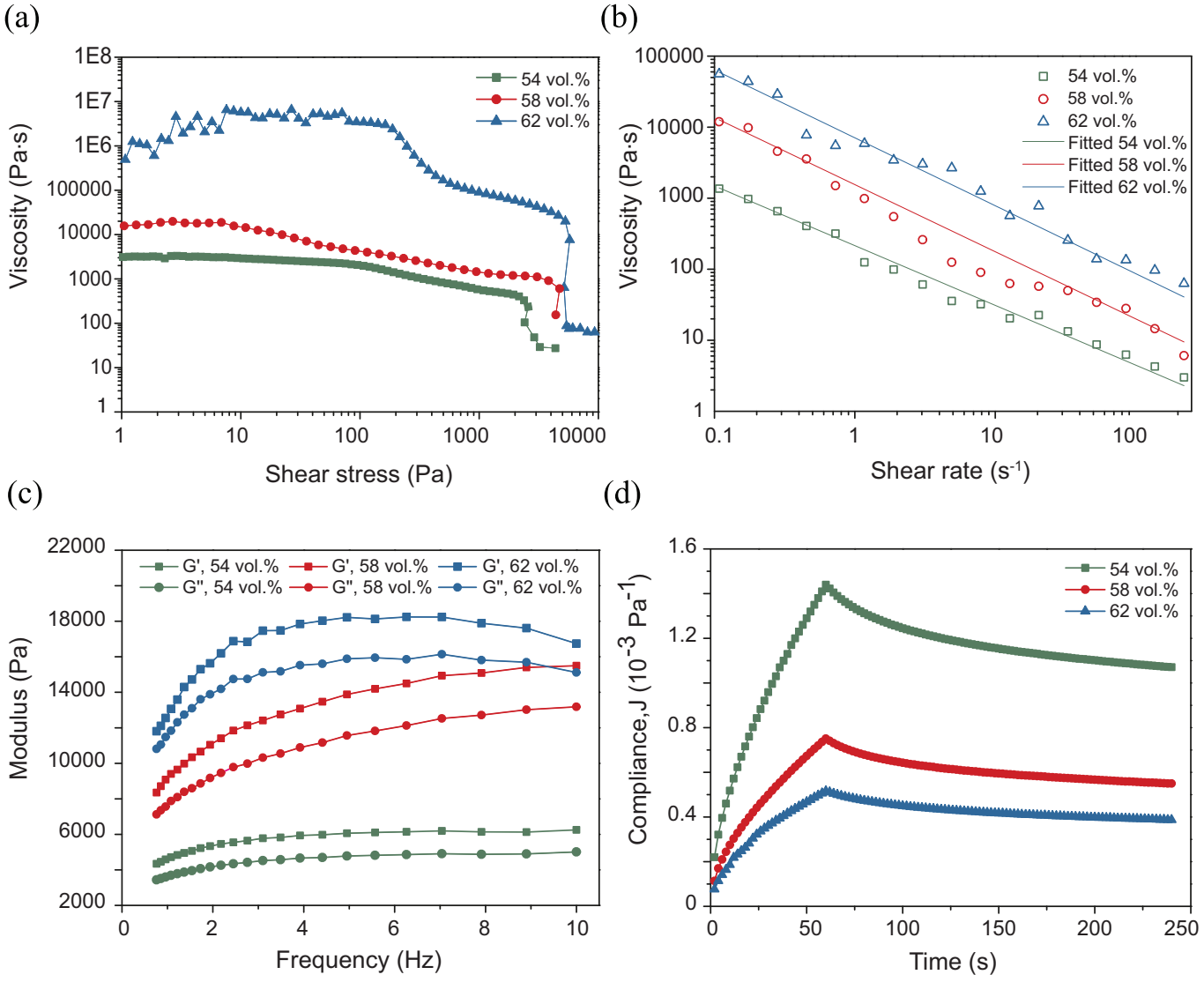

Fig. 3. The rheological characteristics of the Mg powder loaded inks: (a) the results obtained from the shear stress sweep tests at 1 Hz, (b) the results obtained from the shear rate sweep tests at 10 kPa, (c) the *G'* and *G''* values determined from the frequency-sweep tests, and (d) the compliance values determined from the creep-recovery tests.

We used the measured flow rates to calculate the predicted shear rates and subsequently the corresponding viscosity values (at the point when the inks were extruded through the nozzle) using Eq. 3 (Table 2). Clearly, the shear rate is dependent on the flow rate at a given external pressure. An increase in the applied pressure results in a significant increase in the shear rate, accompanied by a decrease in viscosity (Table 2).

Three separate operating windows (Fig. 4b) were defined as guidelines for selecting the printing process parameters (applied pressure and printing speed) for the designed Mg scaffolds with different percentages of Mg powder loading. In each plot, four regions are presented, in which scaffolds with different qualities can be obtained. Zone I indicates that one dimensional (1D) struts with widths in the range of 300 to 500 μm and 2D array can be successfully fabricated. As part of zone I, zone II represents the real printable region for 3D printed Mg scaffolds, while zone III and zone IV represent the unprintable regions, in which the widths of struts were out of the defined range of 300–500 μm as a result of the mismatch of printing parameters.

Several combinations of the process parameters selected from the different zones were adopted for 3D printing trials and the resulting specimens were considered as the representatives of the regions (Fig. 4b). The struts printed with the process parameters at point A in zone IV were much thinner than the expected struts (Fig. 5a) and the lower applied pressure (or higher printing speed) resulted in the displacement of the deposited struts. On the other hand, point C selected in zone III led to the fabrication of much thicker struts (Fig. 5c) and the closure and fusion between adjacent struts. Point B in zone I enabled the successful fabrication of 1D struts or 2D arrays with a desired gap between two struts, without any displacements or fusions (Fig. 5b). The green scaffold samples fabricated with the process parameters at point D in the zone I of the 54 and 58 vol% windows had a collapsed surface with a large degree of deflection (Fig. 5d), while the scaffold samples printed with the process parameters at point F in Zone I of the 58 and 62 vol% windows possessed excessive defects (Fig. 5f). The SEM image of the scaffold fabricated with the process parameters at point E in zone II of the three ink windows

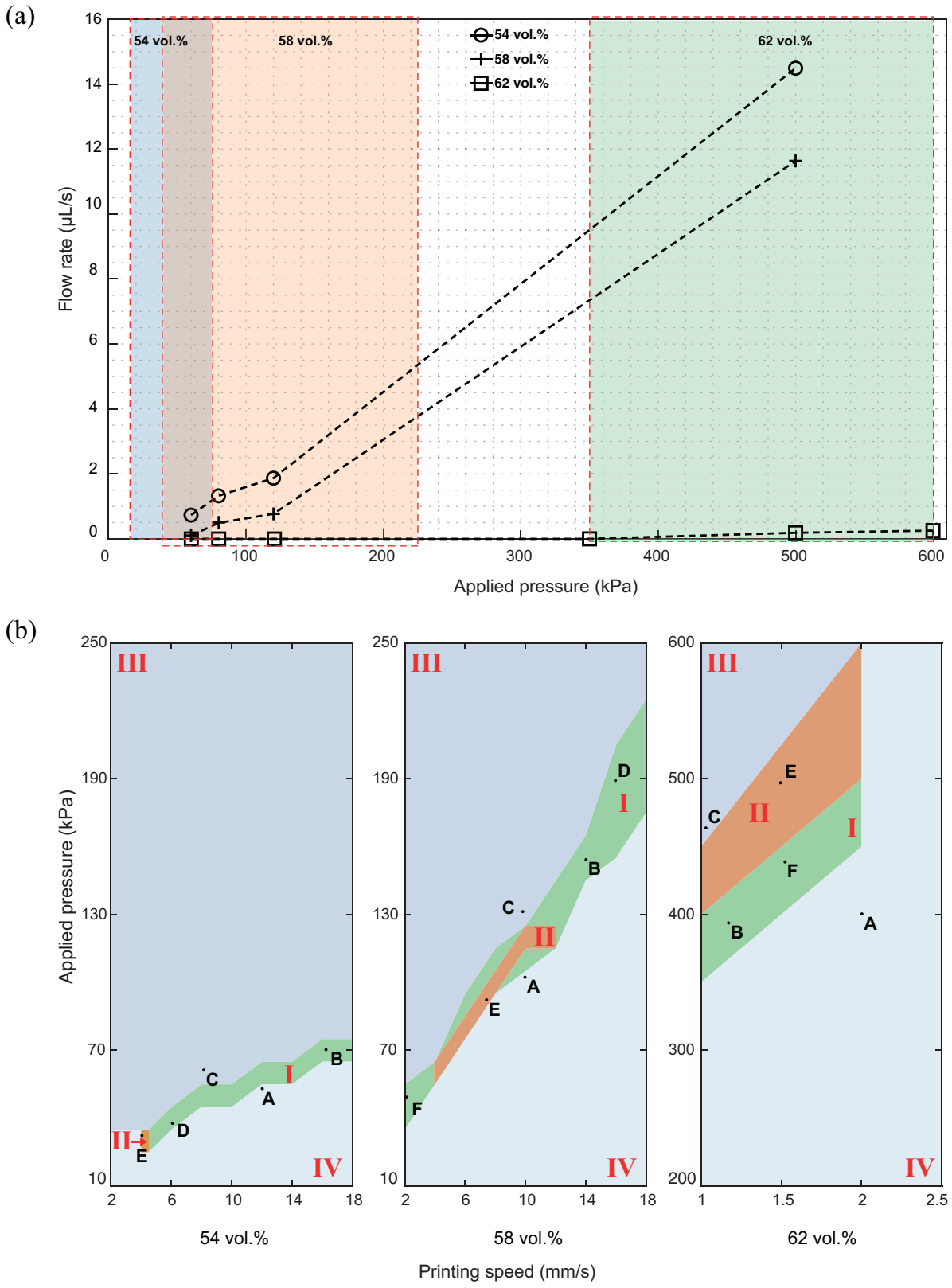

Fig. 4. The characteristic printing behavior of the Mg powder loaded inks: (a) flow rate as a function of the applied pressure* and (b) the printability windows (II: 3D printable zone; I: 2D printable zone; III and IV: unprintable zones).

*The standard deviations of the flow rate values measured were all less than 1%.

Table 2
Predicted shear rate values and corresponding viscosity values during the extrusion of the inks at different applied pressures.

Ink		80 kPa	120 kPa	500 kPa
54 vol%	Shear rate (s^{-1})	$419 \pm 17^{a\ 1}$	$589 \pm 12^{b\ 1}$	$4598 \pm 10^{c\ 1}$
	Viscosity (Pa·s)	$1.70 \pm 0.05^{a\ 1}$	$1.29 \pm 0.02^{b\ 1}$	$0.24 \pm 0.00^{c\ 1}$
58 vol%	Shear rate (s^{-1})	$358 \pm 2^{a\ 2}$	$559 \pm 84^{b\ 1}$	$8459 \pm 98^{c\ 2}$
	Viscosity (Pa·s)	$5.23 \pm 0.02^{a\ 2}$	$3.46 \pm 0.50^{b\ 2}$	$0.26 \pm 0.00^{c\ 1}$
62 vol%	Shear rate (s^{-1})	$0^{a\ 3}$	$0^{a\ 2}$	$159 \pm 2^{b\ 3}$
	Viscosity (Pa·s)	$\infty^{a\ 3}$	$\infty^{a\ 3}$	$54.94 \pm 0.50^{b\ 2}$

a–c: different lowercase letters represent statistically significant differences between the groups of different applied pressures at $p < 0.05$ (comparison in raw);
1–3: different Arabic numbers represent statistically significant differences between the groups of different percentages of Mg powder loading at $p < 0.05$ (comparison in column);
The same letter or number indicates that the values are not significantly different.

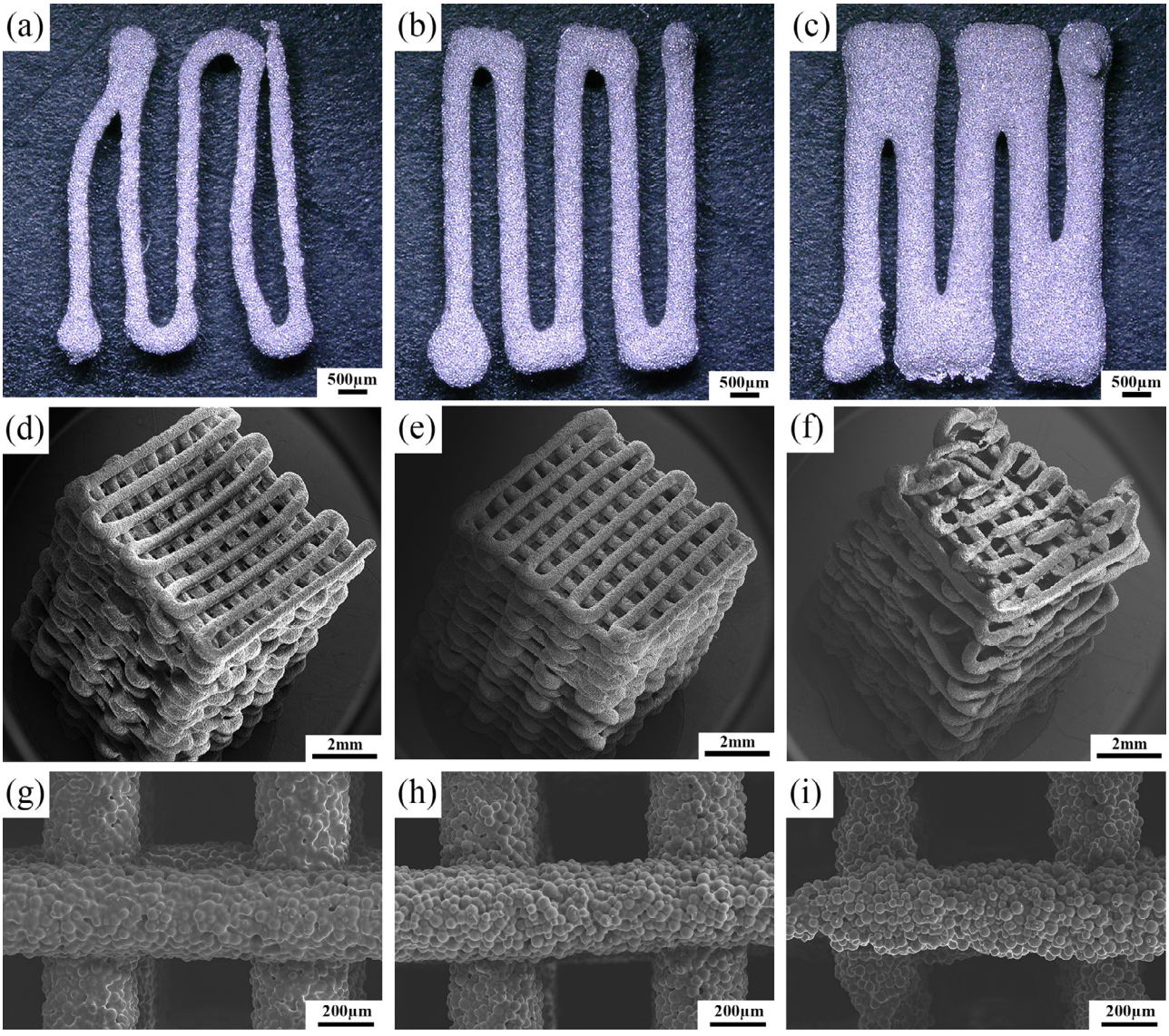

Fig. 5. The results obtained from the printing trials of Mg scaffolds: (a)–(c) printed single-layer struts with the printing process parameters corresponding to points A–C in the printability windows (Fig. 4), respectively, (d)–(f) the representative samples showing samples with deflected surface, accurate alignment and excessive defects, printed with the process parameters corresponding to points D-F in the printability windows (Fig. 4), respectively, and (g),(h) the microstructures of the printed struts initially with 54, 58, and 62 vol% Mg powder loading, respectively.

Table 3
Relative density values of struts after sintering under different conditions.

Sintering temperature (°C)/dwelling time (min)	650/35	650/10	650/5	660/5	670/5
Relative density of struts	70% ± 6%[a]	61% ± 4%[b]	54% ± 6%[c 1]	58% ± 7%[12]	63% ± 7%[2]

a–c: different lowercase letters represent statistically significant differences between the groups of different sintering times at $p < 0.001$.
1–2: different Arabic numbers represent statistically significant differences between the groups of different sintering temperatures at $p < 0.001$;
The same letter or number indicates that the values are not significantly different.

showed that the adjacent layers cohered well together and the struts aligned accurately (Fig. 5e).

The differences in macro-morphology between the struts printed from the inks with 54, 58, and 62 vol% Mg powder loading could be observed through the close-up views of the struts in the scaffolds (Fig. 5g-i). As compared to 58 vol% struts (Fig. 5h), in the 54 vol% struts, Mg powder particles were well covered and bonded by excessive binder (Fig. 5g), while the surface of 62 vol% struts was rough due to insufficient coverage by the binder (Fig. 5i).

The macrographs of the printable scaffold samples (Fig. 5e) showed that the top layer of struts perpendicularly stacked on the layer underneath accurately. Furthermore, there was an overhung part outside the outermost wall of the scaffolds, which was printed without any additional supporting structure. It did not bend or deform during 3D printing or subsequent handling. The shrinkage of the printed scaffold samples was less than 5%, as compared with the designed structure.

3.4. Debinding and sintering

3.4.1. Debinding

TGA of pure binder without Mg powder added revealed two-step weight losses (Fig. 6a). The binder was almost totally decomposed after being heated up to 410 °C and thus above 410 °C, the curve remained steady. FTIR analysis showed that at room temperature, there was no new peak appearing in the spectrum of the ink with 58 vol% Mg powder loading after the Mg powder was added to the binder solution (Fig. 6c), as compared with the spectrum of pure binder. With increasing temperature, TGA of the as-printed sample with 58 vol% Mg powder loading (Fig. 6b) showed a similar trend to that of pure binder (Fig. 6a). The first step of thermal decomposition started to occur at around 115 °C and progressively continued to 210 °C, indicating the removal of plasticizers. Indeed, the peaks stemming from the plasticizers disappeared in the FTIR spectrum of the material after the green samples had been heated to 220 °C, corresponding to the first step debinding, as compared to the spectrum of the ink at room temperature. The leftover peaks at 1492, 1452, 743, and 679 cm^{-1} corresponded to the characteristic absorption frequencies of backbone polymer (Fig. 6c). The second step of binder decomposition occurred in the range of 320 to 440 °C, where the pyrolysis of polymer occurred with the evidence of the absence of the absorption bands that displayed after the material was heated to 220 °C (Fig. 6c). The total weight loss of the 58 vol% Mg powder loaded sample between 115 and 440 °C was found to be around 20 wt%. As compared with the spectrum of the sintered Mg powder without binder, there were no differences between the scaffolds and pure Mg powder samples heated to 650 °C. Due to the absence of vibrations or rotations of organic groups in these samples, both of them showed a nearly steady spectrum (Fig. 6c).

Unlike the TGA curve of the as-printed sample, the TGA curves of the as-received Mg powder and as-sintered samples did not show any pronounced two-step weight losses, but maintained the weight percentage at around 100% before being heated up to 400 °C (Fig. 6b), indicating the absence of the binder in the sintered scaffolds. Above the debinding temperature, the TGA curves of all the three samples showed slight increases prior to decreasing. TGA of the as-received Mg powder and the as-printed sample revealed a weight gain of 6.5 ± 1.3 wt% over a temperature range of 400 to 630 °C and a weight gain of 2.0 ± 0.3 wt% ($p < 0.01$, compared to the as-received Mg powder group), respectively, while the weight gain of the as-sintered Mg sample started from 500 °C and ended at 625 °C with a weight gain of 2.8 ± 0.4 wt% ($p < 0.01$, compared to the as-received Mg powder group) (Fig. 6b). XRD showed that only the pure Mg phase was present in the as-received Mg powder and in the as-printed Mg sample, while in addition to the pure Mg phase, 1–2 wt% MgO phase was detected in the as-sintered sample (Fig. 6d). From the elemental carbon measurement, there was 0.056 ± 0.004 wt% carbon residue in the sintered Mg samples after sintering at 650 °C, compared to 0.011 ± 0.006 wt% carbon measured from the as-received Mg powder ($p < 0.001$).

3.4.2. Sintering

The effects of the sintering temperature and time on the fidelity of sintered 58 vol% Mg powder loaded scaffolds and the sintering neck evolution within struts were examined under SEM and optical microscope. During sintering at 650 °C, necks formed within struts in scaffolds (Fig. 7a2–e2). The sintering results of the Mg scaffolds affected by the sintering temperature and time could be seen from the cross-section close-up micrographs of the struts (Fig. 7a4–e4). Near-net struts were created with necks formed between Mg powder particles and the relative density of struts (excluding the nodules to be described below) increased with increasing holding time and sintering temperature (Table 3).

Interparticle neck formation proceeded greatly after sintering at 650 °C for 35 min and some powder particles were found to have merged together to form a larger body (Fig. 7a2). Reducing the holding time enabled the alleviation of the merging phenomenon of Mg powder particles, but interparticle necks were still well maintained. The growth of necks, the reduction of micro-pores, and powder particle merging tended to progress further as the sintering temperature increased (Fig. 7d2 and e2).

Due to the excessive flow of molten Mg and poor wettability between molten Mg and solid Mg powder particles, some nodules appeared in the fabricated Mg scaffolds (Fig. 7a1–e1) sintered under certain sintering conditions. Large nodules could be found on the surface of the struts and between the struts of the scaffolds sintered at 650 °C for 35 min (Fig. 7a1). The nodules could be large enough to fill the space or macropores between adjacent struts, which could be observed from the cross-section view of the sintered samples (Fig. 7a3). The size of the nodules decreased as the holding time decreased, while no nodules were observed when the holding time was only 5 min (Fig. 7c1–c4). However, they appeared when the temperature was increased from 650 to 660 °C and even to 670 °C, although the holding time was only 5 min (Fig. 7d1 and Fig. 7e3). Many of the macropores between the struts were filled by spherical nodules after sintering at 670 °C, adversely affecting the scaffold fidelity (Fig. 7e3).

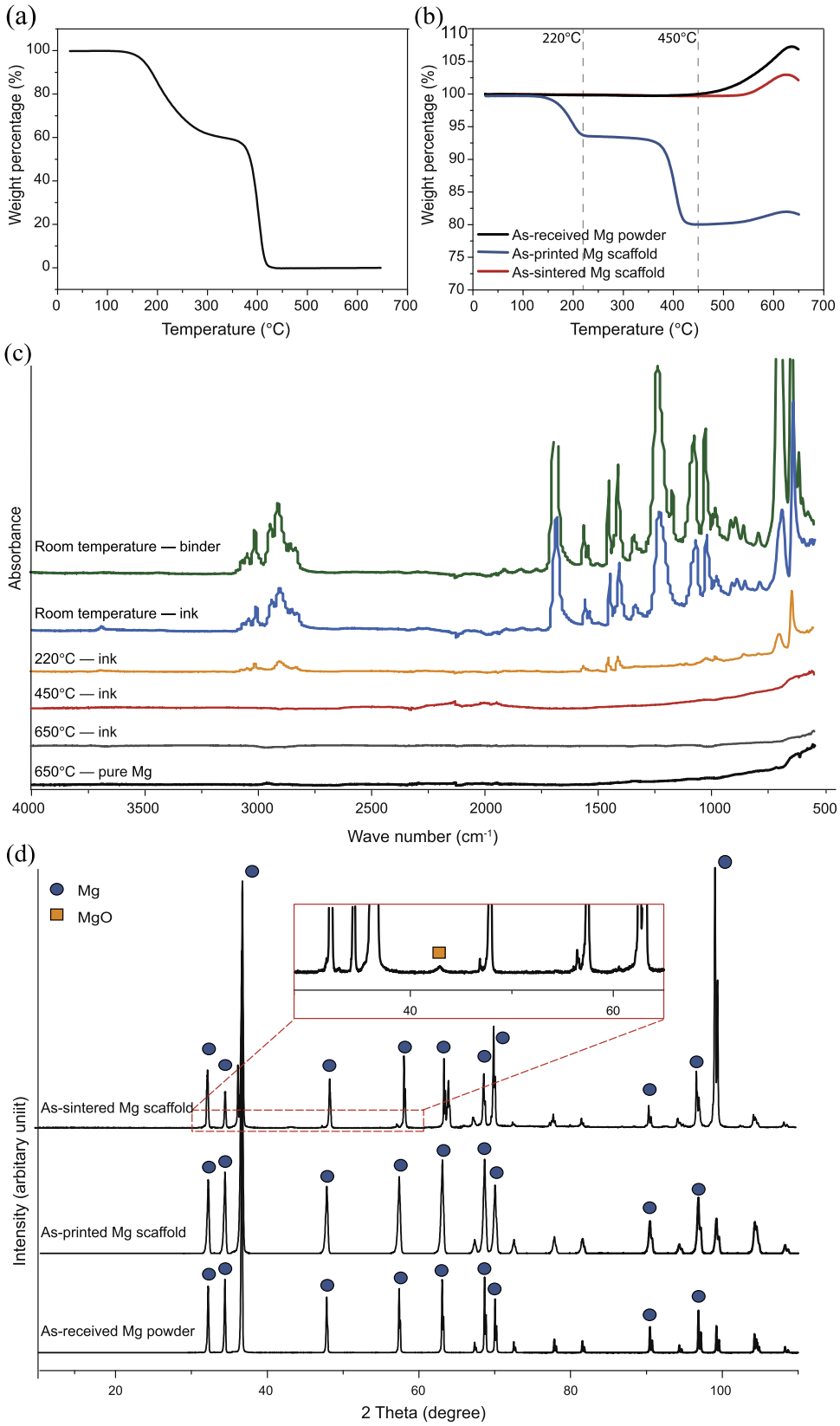

Fig. 6. The characteristics of the decomposition and interaction in the 58 vol% Mg powder loaded scaffold during fabrication process: (a) TGA results of pure binder, (b) TGA results of as-received Mg powders, as-printed and as-sintered scaffolds, (c) FTIR analysis results after the ink was subjected to heating at different temperatures and (d) XRD results of as-received Mg powders, as-printed and as-sintered scaffolds.

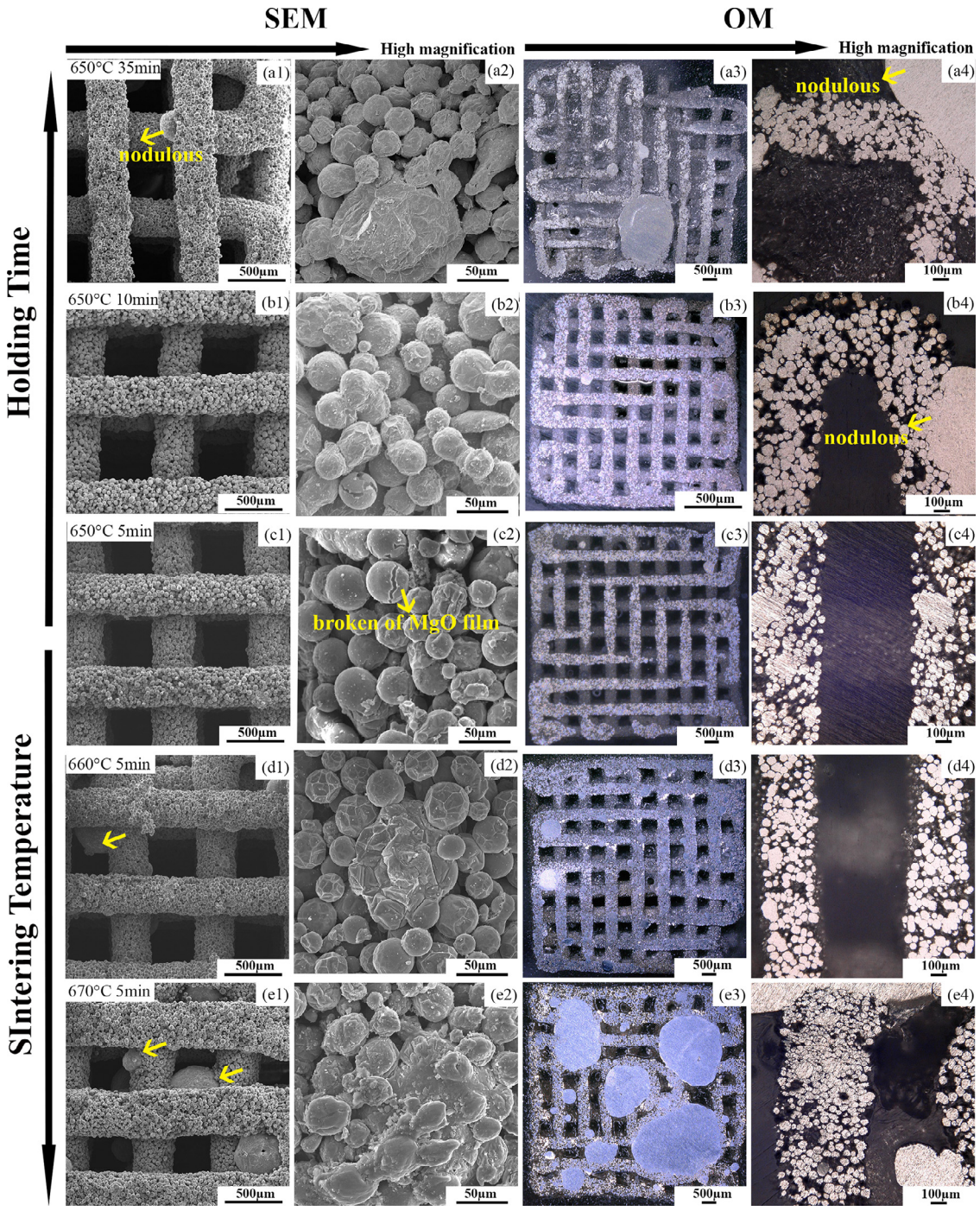

Fig. 7. The sintering behavior and fidelity of the scaffolds initially with 58 vol% Mg powder loading in relation to sintering temperature and holding time.

3.4.3. Hierarchical structure of scaffolds

The macrograph of the sample after sintering at 650 °C for 5 min (Fig. 8b) showed the retention of the shape with high fidelity as compared to the 3D printed sample (Fig. 8a). The strut size after sintering was 323 ± 15 μm. The designed macropores remained open after sintering, as confirmed by the 3D reconstruction of μCT images (Fig. 8c). The pore size was 476 ± 11 μm. The micro-channels and surrounding necks within the struts were clearly visible from the reconstructed models (Fig. 8c) and the micropores in the struts were in a range of 19 to 100 μm according to the calculation of ROI from the μCT images. The porosity of the sintered samples was 78.4%. Both macropores and micropores are mostly interconnected (Fig. 8c). The shrinkage of the sintered sample, relative to the 3D printed sample, was 2.0 ± 0.8%.

4. Discussion

In this study, for the first time, an extrusion-based 3D printing technique was utilized to manufacture porous Mg scaffolds. The major challenges involved in applying this technique, namely the limited number of binder choices and poor sinterability in the absence of external pressure, were overcome. These achievements open up many possibilities to exploit this approach further.

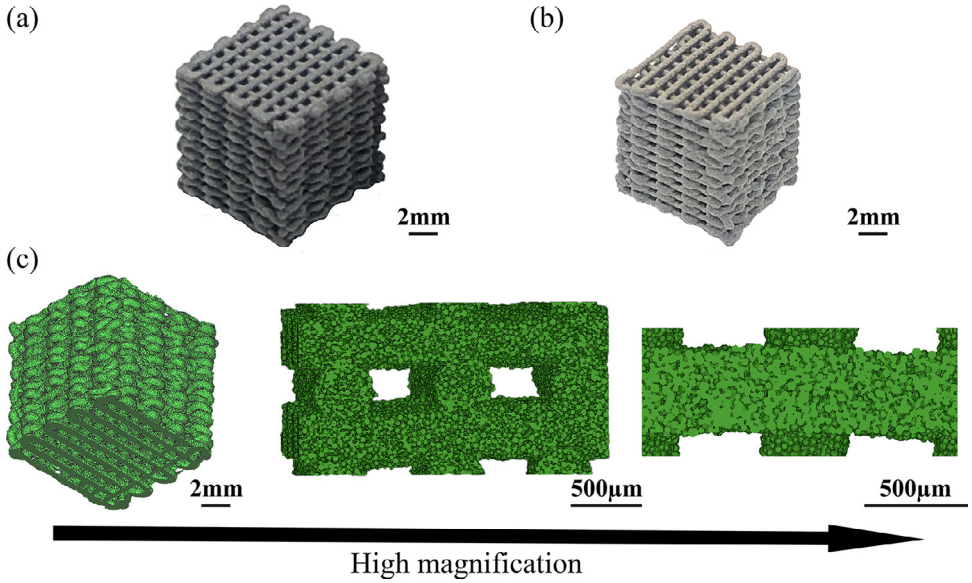

Fig. 8. The macrographs of the fabricated samples: (a) 3D printed sample, (b) sample sintered at 650 °C for 5 min, and (c) reconstructed sintered sample from μCT images.

4.1. Ink preparation

The core of fabricating Mg scaffolds through the SC-3DP process is the design of Mg powder loaded inks that should be chemically stable and exhibit required rheological properties to allow the 3D printing of defect-free Mg scaffolds under ambient conditions. The selection of binder, the rheological properties of the ink, and the relationship between the ink and printing process are discussed below.

4.1.1. Selection of binder

The selection of a proper binder is a challenging task and also a critical step prior to the fabrication of Mg-based scaffolds with the SC-3DP technique. First, considering the intrinsic properties of Mg powder, any water-based binder should be excluded. That is because Mg powder reacts with an aqueous binder and produces a great amount of hydrogen in the ink feedstock. Bubbles were easily observed when Mg powder was mixed with a water-based PVA binder (Fig. S1, see the Supplementary material), which resulted in discontinuous extrusion and severe defects in the manufactured struts. Second, any possible interactions between the Mg powder and the by-products of polymeric binder during debinding should be carefully considered. For instance, commercially available PLGA (polylactide-co-glycolide) has been widely utilized as a binder in combination with volatile solvents for producing various other materials, such as iron [43], nickel-based alloys [45,46], tungsten [49], graphene [50], and ceramic [51] using the SC-3DP technique. In the case of the Mg powder loaded ink with PLGA as the binder, however, we found that during the debinding process, either the ester group (-COOH-) of PLGA or thermally-evolved PLGA fragments adhered to the surfaces of Mg powder particles inevitably containing the hydroxyl (-OH) group, probably leading to the formation of an intermediate compound, magnesium carboxylate (Fig. S2, see the Supplementary material). Similar reactions were found on the surfaces of the alumina [52] and lead titanate [53] samples where poly (methyl methacrylate) (also containing the ester group) was involved. This reaction produced organic residues anchored on Mg powder particle surfaces (Fig. S3, see the Supplementary material), resulting in the retention of non-volatile char on Mg powder particle surfaces and hindering the sintering of Mg powder, although metal carboxylate was not stable at high temperatures.

Finally, apart from the concerns about the possible interactions between the binder and the Mg powder, the temperature of the pyrolysis process and the amount of binder residue should also be considered, because the applicable sintering temperatures of pure Mg with a melting point of 650 °C are relatively low as compared to those applicable to other metals, such as iron and nickel.

Based on the above considerations and the lessons learned from many experimental trials, we designed a graded volatile binder system that consisted of polymer, volatile solvents, and additives for fabricating Mg scaffolds. From the results obtained from the FTIR analysis and TGA, it was confirmed that this binder system did not react with the Mg powder during 3D printing or debinding. This is because that unlike water-based PVA binder, the solvent we used is a kind of water-free organic solvent, and unlike PLGA containing binder, the backbone polymer used in this study does not include the functional group that might react with Mg powder. After debinding, almost no binder residue retained, which could otherwise have hindered the sintering of Mg (Fig. 6). Moreover, the carbon residue results showed that there is very little carbon residue (0.056%) in the sintered samples. Therefore, the chosen binder system would not affect further sintering process.

4.1.2. Rheological properties of the inks

The viscoelastic properties of a viable ink are of critical importance for the success of the SC-3DP approach. A high degree of shear-thinning behavior is particularly important, which enables the ink material to be extruded through fine nozzles, on the one hand, and to possess a sufficiently high rigidity for shape retention on the other hand [54]. Meeting these criteria requires a proper control of ink formulation and rheological properties to generate a stable suspension that promotes the “fluid-to-gel” transition, thereby ensuring the retention of the printed shape and the fusion with the previously deposited layer. The fluid-to-gel transition can be achieved by applying different approaches to different 3D printing techniques, such as temperature-controlled transition [55,56], gelling of precursor solution [57], and solvent evaporation, which was applied to the present printing technique (*i.e.*, SC-3DP). Solvent evaporation is the most commonly used approach for increasing the rigidity of materials right after extrusion, and offers a number of benefits, such as simplicity, room-temperature

processing, *etc*. In addition, by carefully adjusting the ink composition, tailorable rheological properties of the ink can be obtained to maximize its printability.

Solids loading is commonly used to quantify the amount of suspended solids in a substance. In the present study, this is referred to as the amount of Mg powder loaded into the binder to form feedstock or ink for SC-3DP. The volume fraction of solids loading ($Ø$) is closely related to the viscosity of a spherical particle loaded ink [58]. When $Ø$ increases towards a maximum packing fraction ($Ø_m$), the relative viscosity tends to be infinite and the suspension exhibits yield stress behavior. Usually, spherical particles with unimodal sizes, no matter what their sizes may be, can achieve a typical value of $Ø_m$= 0.64 for a random close-packing [59]. This was confirmed experimentally by printing the 64 vol% Mg powder loaded ink and as expected, its flow was totally hindered even though the maximum pressure of the printer, 600 kPa, was applied. Therefore, 54, 58, and 62 vol% Mg powder loading were used in the present study for the optimization of the solid loading in the inks.

In the present case, the rheological behavior of the inks could be tailored by varying the percentage of Mg powder loading (54, 58, and 62 vol%) (Fig. 3). The results obtained from the shear stress sweep, frequency sweep, and creep-recovery tests all showed the viscoelastic properties of the inks. First, in the shear stress sweep test, the obtained yield stress revealed an "at-rest" viscoelastic characteristic, below which the material behaved as a solid. It is reported that the "yield behavior" really exists in highly filled viscous polymers [59]. A suspension composed of a low-viscosity fluid or equivalently a high concentration of solids (Ø>0.5) usually exhibits a high yield stress that must to be exceeded in order to initiate the flow, which is attributed to the particle interaction forces within materials [59]. However, it has been observed that suspensions with particles larger than 10 μm in diameter (non-colloidal suspensions) or volume fraction less than 0.3 usually do not show a sign of yield stress due to the less significant interaction forces among larger particles. Although Mg powder particles with diameters in a range of 25 to 80 μm were used in this study, the "yield behavior" was obvious for the Mg powder loaded inks (Fig. 3), which was most likely due to the addition of plasticizers to the inks. The plasticizers could activate the surface of solid powder particles and, therefore, increase the interfacial interaction between powder particles [60], which promoted the viscoelastic properties of the Mg powder loaded inks. The yield stress of the ink with a higher percentage of Mg powder loading is higher than that of the ink with a lower percentage of Mg powder loading, indicating that a higher printing pressure is required for initiating the flow of the ink with a higher percentage of Mg powder loading (Fig. 4).

Second, in the frequency sweep test, all the three inks conformed to the $G' > G''$ relationship in the linear region (Fig. 3c). The phase angle, δ ($\tan\delta = G''/G'$), is an indicator of the elastic or viscous behavior of an ink. When δ falls in a range of $0° < \delta < 90°$, the material presents viscoelastic behavior, in which the material with $\delta > 45°$ is more viscous and that with $\delta < 45°$ is more elastic [61]. Therefore, the inks with various percentages of Mg powder loading showed dominantly elastic behavior featured by a phase angle smaller than 45°. In the present study, a minimum elastic modulus G' value that is required to have a midpoint deflection of no greater than 5% of the strut diameter was considered, based on a simple elastic beam model [47]. This assessment was widely adopted by other researchers to evaluate the rigidity of the inks to support the entire structure [61-63]. A minimum G' value of 7.05–7.28 Pa was required, based on the calculation with the ink density values of 1.50–1.55 g/ml for 54–62 vol% Mg powder loading, 410 μm in strut diameter, and 390 μm in spacing distance. The G' values of all the inks obtained from the frequency sweep tests (Fig. 3c) were all more than 4 orders of magnitude larger than the required value and, therefore, theoretically satisfied the criterion.

Finally, the viscoelastic properties of the inks were confirmed by the creep-recovery tests, where a quick viscosity recovery with no shear stress applied was required (Fig. 3d). All the prepared inks showed viscoelastic characteristics with about 25% recovery degree. The shear thinning of the inks is a prerequisite for extrusion-based 3D printing. All the prepared inks exhibited the shear-thinning behavior (Fig. 3c), and the degree of shear thinning did not show large differences between the inks with different percentages of Mg powder loading (Table 1). This agrees with the findings of other researchers, showing that n remains unchanged upon the addition of various volume fractions of spherical solids due to the presence of particulates [64].

The viscosity of the suitable inks for extrusion-based 3D printing varies case by case. In the present study, the shear rates for extruding different inks at various applied pressures were derived from the measured flow rates. The corresponding viscosity values of the inks experiencing extrusion for suitable 3D printing (Fig. 4) were between 1 and 60 Pa·s (Table 2), which is in the same viscosity range as reported before [61].

Although the rheological properties are of help in gaining a fundamental understanding of the printability of the inks, the real printing process is significantly more complex than what can be captured from the shear-viscosity measurements. Nevertheless, rheological evaluation can provide a guideline for initial screening or optimizing the suitable inks prior to time-consuming trials of 3D printing. Indeed, in the present research, the rheological characterization of the prepared inks with three different percentages of Mg powder loading provided theoretical support for describing the printability and printing behavior, which will be discussed in the next subsection.

4.2. 3D printing process

The dimensional accuracy of material deposition during the 3D printing process is strongly dependent on the flow rate of the ink (*i.e.*, the extrusion rate of the ink from the nozzle under an external pressure). The flow rate is influenced primarily by three factors, namely the physical and rheological properties of the ink, the geometry of the nozzle, and user-imposed conditions, such as the temperature, which was not included in the present study. First, under the same applied pressure, the flow rate of the ink with a lower percentage of Mg powder loading was found to be larger than that of the ink with a higher percentage of Mg powder loading (54 vol% > 58 vol% > 62 vol%). That is because the flow rate is usually inversely proportional to viscosity. The viscosity value of the ink at the shear rate induced by extruding was in the ascending order: 54 vol% < 58 vol% < 62 vol% (Table 2). Combined with the printability window (Fig. 4b), the appropriate flow rate for printing struts with a fidelity tolerance below 25% (the width of struts in a range of 300 to 500 μm, when a 410 μm nozzle was used) was at a level of 10^{-4} to 10^{-3} ml/s with printing speeds in a range of 1 to 18 mm/s (Fig. 4a). A wide range of flow rates (*i.e.*, 0.07 nL/s - 4 mL/s) were reported for various inks suitable for extrusion-based 3D printing [65]. The flow rates in the present case were, therefore, considered reasonable. Second, the nozzle size and geometry could affect the flow rate. A tapered nozzle was used for 3D printing in the present study, since it is better suited for achieving high-pressure gradients or higher flow rates than a cylindrical nozzle [66].

The applicable printing parameters are determined by the flow rate of the ink. For a given ink, as flow rate increases at a given printing speed, nozzle size, and geometry, the width of the resultant strands increases. In this case, an increased printing speed is needed to ensure the struts width remains within a desired range.

This correlation can give a reasonable explanation for the inclined region of the printability window, especially zone I for 2D strut printing. The selection of suitable process parameters that could be used for successful fabrication of 3D scaffolds is much stricter than that for 2D printing, since maintaining structural integrity would have to be considered in the 3D printing process (Fig. 4b). Two criteria would have to be met for structural integrity: (i) smooth transitions between adjacent layers, which requires enough liquidity for deposited layers to enable seamless fusion with the subsequent layers, and (ii) enough rigidity of firstly deposited layers to support the whole structure, which requires rapid evaporation of solvents right after extrusion. It was observed that the evaporation of the inks played an important role in meeting these two criteria for building the designed structure without distortions or defects, although the presence of additive (*i.e.*, the remaining low vapor pressure solvent) already imparted the liquidity to a certain extent. At a high printing speed, point D in the 54 and 58 vol% windows led to insufficient evaporation of solvents from the deposited layers, resulting in the slumps of the structure (Fig. 5d). A lower printing speed (for example, point F in the 58 vol% window) or a thin strut resulting from an insufficient applied pressure (point F in the 62 vol% window) resulted in too much drying of the layers and, thus, the unmerged or discontinuous layers with poor adhesion (Fig. 5f). In the printability windows of the 54 and 62 vol% Mg powder loaded inks, the printable zones were located at low printing speeds (below 5 mm/s) for the designed 3D scaffolds (Fig. 4b). The 54 vol% Mg powder loaded ink needed more time for evaporation than the ink with a higher percentage of powder loading to reach the same level of rigidity, because the former had more solvents. A lower printing speed means a longer time for the nozzle to reach the same displacement and, therefore, a longer time for the evaporation of the deposited struts before the deposition of next layers. By contrast, the applicable printing speed for the ink with 62 vol% Mg powder loading was limited to a very low speed due to a very low flow rate. In comparison with the inks with 54 and 62 vol% Mg powder loading, the ink with 58 vol% Mg powder loading could be printed over the widest range of printing speeds (*i.e.*, 4–12 mm/s).

In summary, the flow rate (affected by the applied pressure), the evaporation rate (a physical property of the ink) and the deposition rate (determined by printing speed) must be matched with each other for printing the desired 3D structure successfully. The established operating window can be used as a quick guidance for fabricating 3D porous scaffolds with structure sizes on a millimeter scale. It is important to note that the operating window depends on the size and geometry of the designed structure in the evaporation-controlled printing process. In the present study, the printed structure showed a high fidelity without defects and the side pores remained open even over a long spanning length (Fig. 8a). The main limitation of the printing process is that the inks must be printed within 1.5–2 h after having been loaded into the cartridge due to the continuous evaporation of the inks in the cartridge and, thus, an altered viscosity that could affect the printing process.

Apart from the considerations regarding the printability of Mg powder loaded inks, a higher percentage of Mg powder loading is beneficial for the subsequent step (*i.e.*, debinding and sintering), as a high relative density of struts can be obtained and the retention of strut/scaffold shape can be ensured after binder removal. However, the ink with 62 vol% Mg powder loading is not the most promising one, because of its narrow printability window and low printing efficiency (*i.e.*, the low permissible printing speeds). Therefore, the printed scaffolds with 58 vol% Mg powder loading were chosen for further study on the debinding and sintering behavior of the scaffolds.

4.3. Debinding and sintering

Debinding and sintering of porous Mg scaffolds are even more challenging than the 3D printing step. The main challenge involved in debinding is mostly related to the binder selection that has already been discussed earlier. TGA and FTIR analysis (Fig. 6) confirmed the proper choice of the binder, as the vast majority of the binder had been degraded before reaching the sintering temperature and no interaction was found between the reactive Mg powder and the pyrolysis products of the binder during the debinding process.

Apart from the advantages of the seamless attachment of layers during 3D printing, a binary-component binder system is also beneficial for debinding. The plasticizer was removed first to open the paths for further diffusion of the degraded gaseous products (Fig. 6). The major polymer, which served as backbone, retained the strut shape until being almost totally decomposed before the sintering temperature, 650 °C, was reached, with low ash residue (Fig. 6). Around 20 wt% of the binder was thermally decomposed during the 2-step degradation, which was nearly all the binder in the initial feedstock (Fig. 6b). As the backbone polymer was mostly removed before 450 °C was reached, the ash or carbon residue content was of paramount importance for retaining the shape and preventing the scaffolds from slumping and distorting before the formation of the inter-particle necks occurred during sintering. Such a strategy (*i.e.*, a multi-component binder system) is often used in the debinding of metal injection molding (MIM) [67]. A heating rate of 5 °C/min was chosen for debinding and sintering, which was relatively high as compared with that typically applied in MIM. In general, a high heating rate is not preferred in MIM because integrity lose may occur during the debinding process when sudden evaporation of a binder fraction occur with no clear exit path. In solvent-cast 3D printing applied in the present study, however, the backbone binder accounted only for 37 vol% of the binder and the rest were solvent and plasticizer. As a result, the evaporation of the solvent and the decomposition of plasticizer provided sufficient path for the evaporation of polymer. Sudden internal stress that may cause the collapse of the structure would unlike occur. In addition, the carbon residue on the surfaces of Mg powder particles played a vital role in increasing the fiction between Mg powder particles. In other studies on solvent-cast 3D printing of metals, scaffolds could be fabricated successfully even at a heating rate of 10 °C/min during the debinding process [45,46]. Considering a relatively long debinding time being typical in MIM, a single-step protocol was employed in the present study by combining debinding and sintering, during which no dwelling time for debinding was allocated. The relatively quick debinding might be attributed to the pressure-free thin struts that enabled fast diffusion paths for pyrolysis products to move to the green body surfaces where the decomposed binder under argon gas flow could quickly escape [69]. This one-step treatment greatly increased the fabrication efficiency and reduced the operational complexity, as compared with the usual practice in the case of MIM.

The changes of the Mg powder throughout the fabrication process were also studied. XRD revealed that the Mg powder in the as-printed samples remained the same as the as-received powder in phase constitution (Fig. 6d), which was also confirmed by the FTIR results (Fig. 6c). In the sintered sample, however, the MgO phase was found. In TGA, above 400 °C, weight gain occurred to all the tested samples (Fig. 6b) due to the oxidation of Mg. In another study, it also observed that the oxidation of Mg was accelerated above a critical temperature (*i.e.*, 400 °C) at various heating rates even in an ultra-high-purity Ar gas atmosphere (Ar purity: 99.9999%) [68]. After being heated above 400 °C in TGA, the as-printed sample appeared to be less oxidized (with a weight

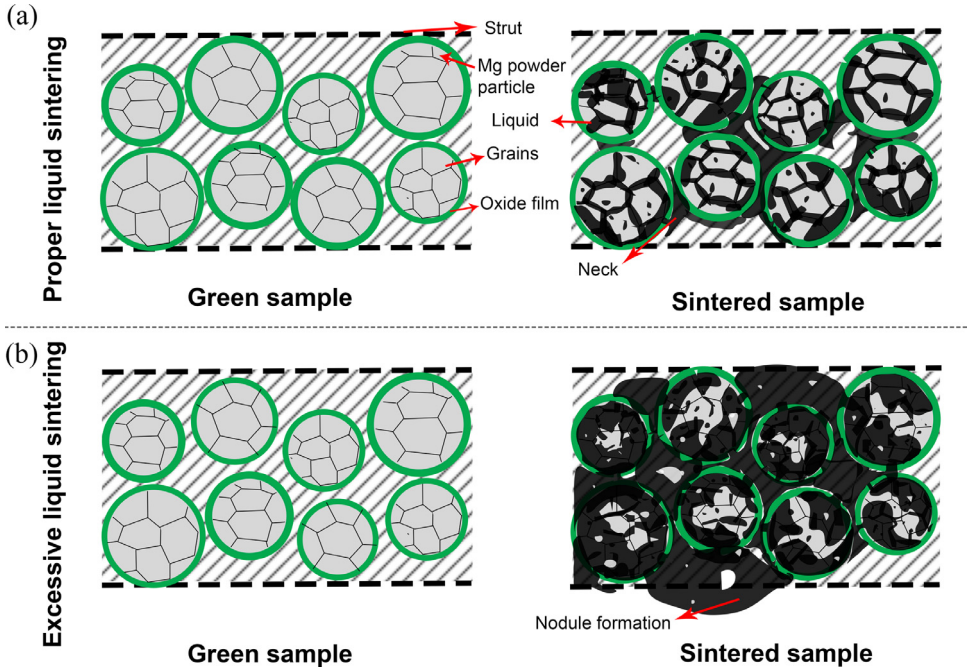

Fig. 9. A schematic illustration of liquid-phase sintering of the Mg 3D scaffolds: (a) proper liquid-phase sintering and (b) excessive liquid-phase sintering.

gain of 2.0 wt%) when compared with pure Mg powder (with a weight gain of 6.5 wt%). This was probably because a small amount of carbon residue from the binder covered some surfaces of Mg powder particles in the as-printed sample, while the as-received Mg powder particles possessed more exposed surfaces. The weight gain of the as-sintered Mg sample was also lower than that of the as-received Mg powder over the temperature range of 400 to 650 °C. This was because the as-sintered Mg sample had already been oxidized once during the sintering process prior to XRD analysis, while pure Mg powder particles still had "relatively clean" surfaces to react with oxygen during XRD test. Therefore, compared with the as-received pure Mg powder, the Mg powder in the as-printed Mg scaffolds did not change chemically after being mixed with the binder, while that in the as-sintered Mg scaffolds presented only small increases in MgO content (1–2 wt%) and carbon content (0.045 wt%).

Sintering of the porous Mg scaffolds was challenging, as the presence of oxide layers on Mg powder particle surfaces severely retarded the sintering process. Unlike other metals, such as iron and copper [70], the diffusion coefficient of Mg atoms (*i.e.*, 5.25×10^{-24} at 650 °C) through the oxide layer is about 12 orders of magnitude lower than their self-diffusivity (3.01×10^{-12} at 650 °C) [71]. Furthermore, the magnesium oxide (MgO) layer on Mg powder particle surfaces is rather stable even beyond the evaporation temperature of Mg. In addition, there is no real possibility of reducing MgO into Mg during sintering. Therefore, solid-state sintering of loose Mg powder is not feasible and breaking up the oxide layer is the only way to allow for effective sintering kinetics, which will provide paths for the diffusion of Mg atoms. With respect to this, the compaction of Mg powder is usually used in order to mechanically rupture the oxide layer in the conventional powder metallurgy techniques. However, the sintering of the designed porous scaffolds excludes the possibility of applying external mechanical pressure on the 3D printed samples. Nevertheless, liquid hot isostatic pressing (HIP) which has been once tried to consolidate a magnesium alloy solid part [72] may be still applicable.

Liquid-phase sintering offers a possibility for the sintering of loose Mg powder, in which the presence of a small volume fraction of the liquid phase facilitates the disruption of the oxide layer and enhances the diffusion. This strategy has been also utilized in the sintering of ZK60 scaffolds fabricated by powder-bed inkjet 3D printing [71]. The control of the presence of a solid-liquid coexistence zone enabled the liquid fraction in the ZK60 alloy to vary from 14 to 43 vol% over a temperature range of 535 to 610 °C, which gave a wide range for the selection of sintering temperature. In comparison with that Mg alloy, it is much more difficult to take advantage of the formed liquid phase for the sintering of with a liquid monophase zone. That is because sintering at or above the melting point of Mg is necessary to generate the liquid phase, but it involves the risk of disrupting the shape of the specimens and even a total collapse of the scaffolds.

With the above considerations, in the present study, we proposed a short sintering process to overcome the challenge involved in pure Mg sintering. It was found that a 5 min holding time was enough to form inter-particle necks at 650 °C. Generally, 650 °C is the melting point of pure Mg. Although the sintering temperature reached the melting point of Mg, the shape of scaffolds was still well retained without any collapse (Fig. 8), owing to the presence of a MgO film on the surfaces of Mg powder particles. A depicted model (Fig. 9) displays how pure Mg can be successfully sintered within a short holding time. Before the occurrence of sintering, an oxide layer covered Mg powder surfaces, which severely impedes diffusion (Fig. 9a). During heating towards 650 °C, the liquid phase appeared along grain boundaries or some defects inside Mg powder particles. As temperature increased to the melting point of Mg, a greater volume fraction of the liquid phase formed inside powder particles. The volumetric expansion of Mg powder particles caused a gradual increase of internal pressure inside Mg powder particles until the oxide layer ruptured. The cracks on the surface of powder particles (Fig. 7c2) provided short-circuit paths for the interior liquid Mg to seep onto the surfaces of powder particles. The released liquid was then drawn into the inter-particle neck regions due to the capillary force, leading to the formation of necks. In summary, the enveloping MgO film enabled the retention of Mg powder particles and scaffold shape, while the cracks of the MgO film gave the melt a chance to flow out and consequently to form necks.

The fidelity of Mg scaffolds or dimensional precision is of paramount importance. A proper sintering scheme (*i.e.*, 650 °C for 5 min) allowed for the fabrication of the Mg scaffolds with high fidelity (Fig. 8), a high relative density of struts, and suitable macro porosity. The sintered scaffolds did not shrink much, as compared to the printed ones, since voids derived from the evaporation of binder were still visible (Fig. 7c4). In other words, the retention of micropores in the struts resulted in insignificant shrinkage. Although a longer holding time and a higher temperature increased the relative density of struts (Table 2), they led to excessive liquid-phase sintering, which caused the formation of nodules and affected the strut fidelity (Fig. 7a3–e3). A longer holding time caused the melting of more Mg and, thus, the formation of excessive Mg liquid. Apart from more liquid formation, higher sintering temperature also enhanced the flowability of Mg liquid through the cracked MgO envelope due to a decrease in its viscosity [73]. The main reason for the formation of nodules that occupied the designed macro pores between struts was a lack of wetting of the molten Mg on powder particle surfaces. When the volume fraction of the liquid went beyond the capability of the capillary force to draw the whole liquid into the bridges formed in the sintered neck regions between powder particles, the excessive liquid reached the exterior of the struts (Fig. 9b), tending to minimize its surface area by forming ball-shaped nodules (Fig. 7). This phenomenon was also reported in another liquid-phase sintering study [37] and similarly, the balling effect occurred during SLM to fabricate Mg scaffolds [27].

4.4. Hierarchical pore structure

The binder removal and the subsequent formation of necks between Mg powder particles enabled the creation of a micropore structure inside the struts. At the same time, accurate 3D printing and high fidelity achieved in the process of debinding and sintering maintained the designed macro pores between the struts (Fig. 8c). Therefore, the fabricated Mg scaffolds possessed an interconnected and hierarchical pore structure, including macropores (between struts) with sizes of 400–500 μm and micropores with sizes of 20–100 μm (inside struts). In comparison with the SLM technique that can only produce scaffolds with dense struts, the SC-3DP technique developed in the present study, is more attractive given that both macropores and micropores play important roles in bone regeneration. Macropores provide spaces and tunnels for cell adhesion, new blood vessel formation and bone ingrowth. It has been found that implants have better osteogenesis when pore sizes are $>$ 300 μm [74,75]. Other studies have found that pore sizes down to 50 μm are efficient in supporting bone ingrowth [76,77]. Furthermore, the interconnected porous structure allows for cell growth and the transport of nutrients and metabolic waste [75]. Therefore, the porous Mg scaffolds fabricated in this study may have great potential to be used as bone substituting biomaterials that enable the regeneration of bone defects. Considering the structural features of the 3D printed scaffolds, it is worth taking further steps to investigate their mechanical properties, degradation behavior, *in vitro* cell response, and *in vivo* bone regeneration performance.

5. Conclusions

Biodegradable porous Mg scaffolds with interconnected pore structures were successfully fabricated using the SC-3DP approach. Ink characteristics were determined and the parameters for 3D printing, debinding and sintering were optimized. All the prepared inks with 54, 58, and 62 vol% Mg powder loading exhibited viscoelastic behavior with adequate elastic moduli for the fabrication of self-supporting structures and were printable with optimized printing parameters (applied pressure and printing speed). The 58 vol% Mg powder loaded ink possessed a wide printability window for printing 3D periodic lattice structures on a millimeter scale. The binder composed of polymer and additives could be removed from the green body and a highly limited amount of carbon residue was left over after debinding. Sintering at the melting point of pure Mg within a short time was found to be suitable for neck formation and for the final Mg scaffolds with good fidelity and considerable densification. As a result, Mg scaffolds with high porosity and a hierarchical pore structure could be obtained, presenting the possibilities for bone ingrowth. The results obtained from this study provided a new way of fabricating biodegradable Mg scaffolds for orthopedic applications.

Declaration of Competing Interest

The authors declare that they have no known competing financial interests or personal relationships that could have appeared to influence the work reported in this paper.

Acknowledgments

J.D. thanks China Scholarship Council (CSC) for financial support. Ms. Ellen Meijvogel-de Koning at the Faculty of Civil Engineering and Geosciences, Delft University of Technology, is acknowledged for μCT scans. J.D. thanks Mr. Meng Zhang and Ms. Helda Pahlavani for the post-processing of μ-CT data. The assistance of Mr. Hans Brouwer and Mr. Niko Eka Putra during the experiments is also appreciated.

Supplementary materials

Supplementary material associated with this article can be found, in the online version, at doi:10.1016/j.actbio.2020.08.002.

References

[1] V. Campana, G. Milano, E. Pagano, M. Barba, C. Cicione, G. Salonna, W. Lattanzi, G. Logroscino, Bone substitutes in orthopaedic surgery: from basic science to clinical practice, J. Mater. Sci. Mater. Med. 25 (2014) 2445–2461.
[2] S. Bose, M. Roy, A. Bandyopadhyay, Recent advances in bone tissue engineering scaffolds, Trends Biotechnol. 30 (2012) 546–554.
[3] P. Janicki, G. Schmidmaier, What should be the characteristics of the ideal bone graft substitute? Combining scaffolds with growth factors and/or stem cells, Injury 42 (Suppl 2) (2011) S77–S81.
[4] A.A. Zadpoor, Bone tissue regeneration: the role of scaffold geometry, Biomater. Sci. 3 (2015) 231–245.
[5] F. Witte, The history of biodegradable magnesium implants: a review, Acta Biomater. 6 (2010) 1680–1692.
[6] C. Palacios, The role of nutrients in bone health, from A to Z, Crit. Rev. Food Sci. Nutr. 46 (2006) 621–628.
[7] Y. Zhang, J. Xu, Y.C. Ruan, M.K. Yu, M. O'laughlin, H. Wise, D. Chen, L. Tian, D. Shi, J. Wang, S. Chen, J.Q. Feng, D.H. Chow, X. Xie, L. Zheng, L. Huang, S. Huang, K. Leung, N. Lu, L. Zhao, H. Li, D. Zhao, X. Guo, K. Chan, F. Witte, H.C. Chan, Y. Zheng, L. Qin, Implant-derived magnesium induces local neuronal production of CGRP to improve bone-fracture healing in rats, Nat. Med. 22 (2016) 1160–1169.
[8] M.P. Staiger, A.M. Pietak, J. Huadmai, G. Dias, Magnesium and its alloys as orthopedic biomaterials: a review, Biomaterials 27 (2006) 1728–1734.
[9] X.C. Xia, X.W. Chen, Z. Zhang, X. Chen, W.M. Zhao, B. Liao, B. Hur, Effects of porosity and pore size on the compressive properties of closed-cell Mg alloy foam, J. Magnes. Alloy 1 (2013) 330–335.
[10] D.-H. Yang, B.-Y. Hur, S.-R. Yang, Study on fabrication and foaming mechanism of Mg foam using $CaCO_3$ as blowing agent, J. Alloy Compd. 461 (2008) 221–227.
[11] H.J. Luo, L. Zhang, Z.G. Xu, Y.S. Yang, Effect of technological parameters on preparation of Mg-based foam materials, Mater. Sci. Forum 749 (2013) 356–360.
[12] M.P. Staiger, I. Kolbeinsson, N.T. Kirkland, T. Nguyen, G. Dias, T.B.F. Woodfield, Synthesis of topologically-ordered open-cell porous magnesium, Mater. Lett. 64 (2010) 2572–2574.
[13] K. Lietaert, L. Weber, J. Van Humbeeck, A. Mortensen, J. Luyten, J. Schrooten, Open cellular magnesium alloys for biodegradable orthopaedic implants, J. Magnes. Alloy 1 (2013) 303–311.
[14] J.O. Osorio-Hernández, M.A. Suarez, R. Goodall, G.A. Lara-Rodriguez, I. Alfonso, I.A. Figueroa, Manufacturing of open-cell Mg foams by replication process and mechanical properties, Mater. Des. 64 (2014) 136–141.

[15] X. Wang, Z. Li, Y. Huang, K. Wang, X. Wang, F. Han, Processing of magnesium foams by weakly corrosive and highly flexible space holder materials, Mater. Des. 64 (2014) 324–329.
[16] N. Kleger, M. Cihova, K. Masania, A.R. Studart, J.F. Loffler, 3D printing of salt as a template for magnesium with structured porosity, Adv. Mater. 31 (2019) e1903783.
[17] G. Jiang, G. He, A new approach to the fabrication of porous magnesium with well-controlled 3D pore structure for orthopedic applications, Mater. Sci. Eng. C 43 (2014) 317–320.
[18] M.Q. Cheng, T. Wahafu, G.F. Jiang, W. Liu, Y.Q. Qiao, X.C. Peng, T. Cheng, X.L. Zhang, G. He, X.Y. Liu, A novel open-porous magnesium scaffold with controllable microstructures and properties for bone regeneration, Sci. Rep. 6 (2016) 24134.
[19] Y.Z. Bi, Y. Zheng, Y. Li, Microstructure and mechanical properties of sintered porous magnesium using polymethyl methacrylate as the space holder, Mater. Lett. 161 (2015) 583–586.
[20] M.M.C.E. Wen, Y. Yamada, K. Shimojima, Y. Chino, T. Asahina, T. Asahina, Processing of biocompatible porous Ti and Mg, Scr. Mater. 45 (2001) 1147–1153.
[21] G.L. Hao, F.S. Han, W.D. Li, Processing and mechanical properties of magnesium foams, J. Porous Mater. 16 (2008) 251–256.
[22] J. Capek, D. Vojtech, Properties of porous magnesium prepared by powder metallurgy, Mater. Sci. Eng. C 33 (2013) 564–569.
[23] O. Al-Ketan, R. Rowshan, R.K. Abu Al-Rub, Topology-mechanical property relationship of 3D printed strut, skeletal, and sheet based periodic metallic cellular materials, Addit. Manuf. 19 (2018) 167–183.
[24] X.Y. Zhang, G. Fang, J. Zhou, Additively manufactured scaffolds for bone tissue engineering and the prediction of their mechanical behavior: a review, Materials 10 (2017) 50.
[25] Y. Qin, P. Wen, H. Guo, D. Xia, Y. Zheng, L. Jauer, R. Poprawe, M. Voshage, J.H. Schleifenbaum, Additive manufacturing of biodegradable metals: current research status and future perspectives, Acta Biomater. 98 (2019) 3–22.
[26] S. Gangireddy, B. Gwalani, K. Liu, E.J. Faierson, R.S. Mishra, Microstructure and mechanical behavior of an additive manufactured (AM) WE43-Mg alloy, Addit. Manuf. 26 (2019) 53–64.
[27] V. Manakari, G. Parande, M. Gupta, Selective laser melting of magnesium and magnesium alloy powders: a review, Metals 7 (2016) 2.
[28] N.A. Zumdick, L. Jauer, L.C. Kersting, T.N. Kutz, J.H. Schleifenbaum, D. Zander, Additive manufactured WE43 magnesium: A comparative study of the microstructure and mechanical properties with those of powder extruded and as-cast WE43, Mater. Charact. 147 (2019) 384–397.
[29] D. Hu, Y. Wang, D. Zhang, L. Hao, J. Jiang, Z. Li, Y. Chen, Experimental investigation on selective laser melting of bulk net-shape pure magnesium, Mater. Manuf. Process. 30 (2015) 1298–1304.
[30] C. Chung Ng, M. Savalani, H. Chung Man, Fabrication of magnesium using selective laser melting technique, Rapid Prototyp. J. 17 (2011) 479–490.
[31] H. Takagi, H. Sasahara, T. Abe, H. Sannomiya, S. Nishiyama, S. Ohta, K. Nakamura, Material-property evaluation of magnesium alloys fabricated using wire-and-arc-based additive manufacturing, Addit. Manuf. 24 (2018) 498–507.
[32] J. Guo, Y. Zhou, C. Liu, Q. Wu, X. Chen, J. Lu, Wire arc additive manufacturing of AZ31 magnesium alloy: grain refinement by adjusting pulse frequency, Materials 9 (2016) 823.
[33] Y. Li, J. Zhou, P. Pavanram, M.A. Leeflang, L.I. Fockaert, B. Pouran, N. Tumer, K.U. Schroder, J.M.C. Mol, H. Weinans, H. Jahr, A.A. Zadpoor, Additively manufactured biodegradable porous magnesium, Acta Biomater. 67 (2018) 378–392.
[34] A. Kopp, T. Derra, M. Muther, L. Jauer, J.H. Schleifenbaum, M. Voshage, O. Jung, R. Smeets, N. Kroger, Influence of design and postprocessing parameters on the degradation behavior and mechanical properties of additively manufactured magnesium scaffolds, Acta Biomater. 98 (2019) 23–35.
[35] S. Das, Physical aspects of process control in selective laser sintering of metals, Adv. Eng. Mater. 5 (2003) 701–711.
[36] Y. Yang, P. Wu, X. Lin, Y. Liu, H. Bian, Y. Zhou, C. Gao, C. Shuai, System development, formability quality and microstructure evolution of selective laser-melted magnesium, Virtual Phys. Prototyp. 11 (2016) 173–181.
[37] M. Salehi, S. Maleksaeedi, M.L.S. Nai, M. Gupta, Towards additive manufacturing of magnesium alloys through integration of binderless 3D printing and rapid microwave sintering, Addit. Manuf. 29 (2019) 100790.
[38] M. Wolff, T. Mesterknecht, A. Bals, T. Ebel, R. Willumeit-RöMer, FFF of Mg-alloys for biomedical application. Materials technology symposium, in: Proceedings of the 148th TMS Annual Meeting, San Antonio, Texas, 2019.
[39] S.Z. Guo, M.C. Heuzey, D. Therriault, Properties of polylactide inks for solvent-cast printing of three-dimensional freeform microstrcutures, Langmuir 30 (2014) 1142–1150.
[40] C. Xu, A. Bouchemit, G. L'esperance, L.L. Lebel, D. Therriault, Solvent-cast based metal 3D printing and secondary metallic infiltration, J. Mater. Chem. C 5 (2017) 10448–10455.
[41] C. Xu, Q. Wu, G. L'espérance, L.L. Lebel, D. Therriault, Environment-friendly and reusable ink for 3D printing of metallic structures, Mater. Des. 160 (2018) 262–269.
[42] C. Yang, Z.G. Huan, X.Y. Wang, C.T. Wu, J. Chang, 3D printed Fe scaffolds with HA nanocoating for bone regeneration, ACS Biomater. Sci. Eng. 4 (2018) 608–616.
[43] S.L. Taylor, A.E. Jakus, R.N. Shah, D.C. Dunand, Iron and nickel cellular structures by sintering of 3D-printed oxide or metallic particle inks, Adv. Eng. Mater. 19 (2017) 8.
[44] J.P. Li, J.R. De Wijn, C.A. Van Blitterswijk, K. De Groot, The effect of scaffold architecture on properties of direct 3D fiber deposition of porous Ti6Al4V for orthopedic implants, J. Biomed. Mater. Res. Part A 92A (2010) 33–42.
[45] S.L. Taylor, A.J. Lbeh, A.E. Jakus, R.N. Shah, D.C. Dunand, NiTi-Nb micro-trusses fabricated via extrusion-based 3D-printing of powders and transient-liquid-phase sintering, Acta Biomater. 76 (2018) 359–370.
[46] S.L. Taylor, R.N. Shah, D.C. Dunand, Ni-Mn-Ga micro-trusses via sintering of 3D-printed inks containing elemental powders, Acta Mater. 143 (2018) 20–29.
[47] J.C. James, E. Smay, A. Jennifer, Lewis, Colloidal Inks for directed assembly of 3-D periodic structures, Langmuir 18 (2002) 5429–5437.
[48] M. Doube, M.M. Klosowski, I. Arganda-Carreras, F.P. Cordelieres, R.P. Dougherty, J.S. Jackson, B. Schmid, J.R. Hutchinson, S.J. Shefelbine, Bone J: free and extensible bone image analysis in Image J, Bone 47 (2010) 1076–1079.
[49] M. Calvo, A.E. Jakus, R.N. Shah, R. Spolenak, D.C. Dunand, Microstructure and processing of 3D printed tungsten microlattices and infiltrated W-Cu composites, Adv. Eng. Mater. 20 (2018) 9.
[50] A.E. Jakus, E.B. Secor, A.L. Rutz, S.W. Jordan, M.C. Hersam, R.N. Shah, Three--dimensional printing of high-content graphene scaffolds for electronic and biomedical applications, ACS Nano 9 (2015) 4636–4648.
[51] A.E. Jakus, A.L. Rutz, S.W. Jordan, A. Kannan, S.M. Mitchell, C. Yun, K.D. Koube, S.C. Yoo, H.E. Whiteley, C.P. Richter, R.D. Galiano, W.K. Hsu, S.R. Stock, E.L. Hsu, R.N. Shah, Hyperelastic "bone": a highly versatile, growth factor-free, osteoregenerative, scalable, and surgically friendly biomaterial, Sci. Transl. Med. 8 (2016) 15.
[52] R.J. Higgins, W.E. Rhine, M.J. Cima, H.K. Bowen, Ceramic surface reactions and carbon retention during non-oxidative binder removal: Al_2O_3/poly(methyl methacrylate) at 20°-700°C, J. Am. Ceram. Soc. 77 (1994) 2243–2253.
[53] K. Hirakata, W.E. Rhine, M.J. Cima, Surface chemistry of lead titanate and its impact on binder removal, J. Am. Ceram. Soc. 79 (1996) 1002–1008.
[54] N. Paxton, W. Smolan, T. Bock, F. Melchels, J. Groll, T. Jungst, Proposal to assess printability of bioinks for extrusion-based bioprinting and evaluation of rheological properties governing bioprintability, Biofabrication 9 (2017) 044107.
[55] S. Hong, C. Sanchez, H. Du, N. Kim, Fabrication of 3D printed metal structures by use of high-isvcosity Cu paste and a screw extruder, J. Electron. Mater. 44 (2015) 836–841.
[56] U. Scheithauer, E. Schwarzer, H.-J. Richter, T. Moritz, Thermoplastic 3D printing – an additive manufacturing method for producing dense ceramics, Int. J. Appl. Ceram. Technol. 12 (2015) 26–31.
[57] J.M. Lee, W.Y. Yeong, Design and printing strategies in 3D bioprinting of cell-hydrogels: a review, Adv. Healthc. Mater. 5 (2016) 2856–2865.
[58] M. Mooney, The viscosity of a concentrated suspension of spherical particles, in: Proceedings of Annual Meeting of the Society of Rheology, New York, 1950.
[59] M.M. Rueda, M.C. Auscher, R. Fulchiron, T. Perie, G. Martin, P. Sonntag, P. Cassagnau, Rheology and applications of highly filled polymers: a review of current understanding, Prog. Polym. Sci. 66 (2017) 22–53.
[60] G.Q. Xie, Y.H. Zhang, W.S. Lin, Plasticizer combinations and performance of wood flour–poly(lactic acid) 3D printing filaments, BioResources 12 (2017) 6736–6748.
[61] C.R. Tubio, F. Guitian, A. Gil, Fabrication of ZnO periodic structures by 3D printing, J. Eur. Ceram. Soc. 36 (2016) 3409–3415.
[62] J.A. Lewis, Direct-write assembly of ceramics from colloidal inks, Curr. Opin. Solid State Mater. Sci. 6 (2002) 245–250.
[63] R.B. Rao, K.L. Krafcik, A.M. Morales, J.A. Lewis, Microfabricated deposition nozzles for direct-write assembly of three-dimensional periodic structures, Adv. Mater. 17 (2005) 289–293.
[64] A.J. Poslinski, M.E. Ryan, R.K. Gupta, S.G. Seshadri, F.J. Frechette, Rheological behavior of filled polymeric systems I. Yield stress and shear-thinning effects, J. Rheol. 32 (1988) 703–735.
[65] E.N. Udofia, W.C. Zhou, Microextrusion based 3D printing – a review, in: Proceedings of the 29th Annual International Solid Freeform Fabrication Symposium, TMS, Texas, USA, 2018.
[66] M. Li, X. Tian, D.J. Schreyer, X. Chen, Effect of needle geometry on flow rate and cell damage in the dispensing-based biofabrication process, Biotechnol. Prog. 27 (2011) 1777–1784.
[67] Z.Y. Liu, N.H. Loh, S.B. Tor, K.A. Khor, Y. Murakoshi, R. Maeda, Binder system for micropowder injection molding, Mater. Lett. 48 (2001) 31–38.
[68] M. Salehi, S. Maleksaeedi, H. Farnoush, N.M.L. Sharon, G.K. Meenashisundaram, M. Gupta, An investigation into interaction between magnesium powder and Ar gas: Implications for selective laser melting of magnesium, Powder Technol. 333 (2018) 252–261.
[69] J.A. Lewis, Binder removal from ceramics, Annu. Rev. Mater. Sci. 27 (1997) 147–173.
[70] Z.A. Munir, Analytical treatment of the role of surface oxide layers in the sintering of metals, J. Mater. Sci. 14 (1979) 2733–2740.
[71] M. Salehi, S. Maleksaeedi, M.A.B. Sapari, M.L.S. Nai, G.K. Meenashisundaram, M. Gupta, Additive manufacturing of magnesium–zinc–zirconium (ZK) alloys via capillary-mediated binderless three-dimensional printing, Mater. Des. 169 (2019) 107683.
[72] M.G. Beghi, G. Caglioti, V. Carvelli, C. Poggi, Liquid hot isostatic pressing of QE22A magnesium alloy: a preliminary test, Metall. Res. Technol. 21 (2003) 15–17.
[73] G.B. Mi, P.J. Li, P.S. Popel, I.S. Abaturov, Viscosity of AZ91D magnesium alloy melt with small additions of calcium, Chin. J. Nonferrous Met. 19 (2009) 1372–1378.

[74] V. Karageorgiou, D. Kaplan, Porosity of 3D biomaterial scaffolds and osteogenesis, Biomaterials 26 (2005) 5474–5491.
[75] X.J. Wang, S.Q. Xu, S.W. Zhou, W. Xu, M. Leary, P. Choong, M. Qian, M. Brandt, Y.M. Xie, Topological design and additive manufacturing of porous metals for bone scaffolds and orthopaedic implants: a review, Biomaterials 83 (2016) 127–141.
[76] C.-K.L. Bong-Soon Chang, Choon-Ki Lee, Osteoconduction at porous hydroxyapatite with various pore configurations, Biomaterials 21 (2000) 1291–1298.
[77] F. He, G. Qian, W. Ren, J. Li, P. Fan, H. Shi, X. Shi, X. Deng, S. Wu, J. Ye, Fabrication of beta-tricalcium phosphate composite ceramic sphere-based scaffolds with hierarchical pore structure for bone regeneration, Biofabrication 9 (2017) 025005.